Check for updates

Advanced Materials

ADVANCED MATERIALS
www.advmat.de

RESEARCH ARTICLE OPEN ACCESS

Quantum Saturation of the Electro-Optic Effect

Aiden Ross[1] | Sankalpa Hazra[1] | Albert Suceava[1] | Dylan Sotir[2,3] | Ian Reed Philippi[1] | Darrell G. Schlom[3,4,5] | Venkatraman Gopalan[1] | Long-Qing Chen[1]

[1]Department of Materials Science and Engineering, The Pennsylvania State University, Pennsylvania, USA | [2]Platform for the Accelerated Realization, Analysis, and Discovery of Interface Materials (PARADIM), Cornell University, Ithaca, New York, USA | [3]Department of Materials Science and Engineering, Cornell University, Ithaca, New York, USA | [4]Kavli Institute at Cornell for Nanoscale Science, Ithaca, New York, USA | [5]Leibniz-Institut Für Kristallzüchtung, Berlin, Germany

Correspondence: Aiden Ross (amr8057@psu.edu) | Long-Qing Chen (lqc3@psu.edu)

Received: 16 February 2026 | **Revised:** 15 October 2026 | **Accepted:** 21 October 2026

Keywords: barium titanate | electro-optic effect | ferroelectrics | Pockels effect | quantum optics

ABSTRACT

Future quantum computing architectures require electro-optic materials that maintain a strong, stable performance at cryogenic temperatures. In conventional electro-optic materials, large electro-optic coefficients are often confined to narrow temperature windows near structural phase transitions, where small changes in temperature lead to large changes in the electro-optic response. Using thermodynamic analysis, phase-field simulations, experimental growth, and cryogenic optical measurements, we show that quantum fluctuations can be harnessed to overcome this trade-off. By tuning the ferroelectric phase boundaries down to 0 K, quantum fluctuations induce a saturation regime in which a large electro-optic response becomes nearly temperature-independent below 25 K. We demonstrate that the phase boundaries can be tuned through either strain in $BaTiO_3$ or through chemical composition in $Ba_{1-x}Ca_xTiO_3$, leading to a large, temperature-insensitive, cryogenic electro-optic response, $r_{eff} = 2850\ pm\ V^{-1}$ (experiment) and $r_{51} = 2900\ pm\ V^{-1}$ (theory) for $BaTiO_3$ on $GdScO_3$ and $r_{51} = 1898\ pm\ V^{-1}$ (theory) for $Ba_{0.77}Ca_{0.23}TiO_3$. These values exceed the room temperature performance of bulk $BaTiO_3$ $r_{51} = 1600\ pm\ V^{-1}$ and surpass the cryogenic performance of $BaTiO_3$-on-Si, $r_{eff} = 200\ pm\ V^{-1}$, by over an order of magnitude. These findings establish a general design principle for engineering high-performance electro-optic materials for cryogenic applications.

1 | Introduction

Electro-optic materials play a central role in emerging quantum photonic technologies. As practical quantum computers scale to millions of qubits, they will rely on a modular architecture linking many quantum processors with low-loss and low-noise photonic links [1, 2], made possible by high-performance electro-optic materials that read [3, 4], write [3, 5], and transfer quantum states [6]. These same materials underpin photonic quantum computing platforms [7]. Across all these potential applications a large cryogenic electro-optic effect reduces operating voltages, increases efficiency, and minimizes device footprint.

$BaTiO_3$ has emerged as a promising material for electro-optic devices, with a large electro-optic coefficient (bulk: $r_{51} \sim 1600$ pm V^{-1} [8], film: $r_{51} \sim 900$ pm V^{-1}) [9] at room temperature. Unfortunately, its performance sharply degrades at cryogenic temperatures ($r_{eff} \sim 200$ pm V^{-1}) [9, 10]. Theoretical calculations attribute its large room-temperature electro-optic coefficient to the close competition between different ferroelectric states in the proximity to the tetragonal-to-orthorhombic ferroelectric phase transition [11], leading to a dynamic averaging of lower symmetry monoclinic structures [12]. Nonetheless, this room-temperature response is both highly temperature-dependent and strongly suppressed at cryogenic temperatures due to phase transitions [10, 11, 13]. A central goal is therefore to identify

This is an open access article under the terms of the Creative Commons Attribution License, which permits use, distribution and reproduction in any medium, provided the original work is properly cited.
© 2026 The Author(s). *Advanced Materials* published by Wiley-VCH GmbH

strategies that enhance the electro-optic response of $BaTiO_3$ while simultaneously stabilizing it against variations in temperature.

At low temperatures, quantum fluctuations dominate the behavior of ferroelectrics, giving rise to quantum saturation effects [14]. In quantum paraelectrics, such as $SrTiO_3$ and $KTaO_3$, quantum fluctuations suppress the ferroelectric phase altogether, despite an underlying soft mode instability [15–17]. In $BaTiO_3$, by contrast, quantum fluctuations do not eliminate the ferroelectric phase, but instead suppress changes in the ferroelectric polarization below a characteristic saturation temperature (T_s) [18]. In this quantum-saturated regime, quantum fluctuations dominate over thermal fluctuations, leading to properties which become temperature insensitive [14], presenting a compelling opportunity to realize a large, thermally stable electro-optic response. So far, realizing materials in which a strong electro-optic effect coincides with the quantum saturation regime has remained a challenge. Recent theoretical calculations and experimental measurements have demonstrated the possibility of using epitaxial strain to substantially enhance the cryogenic electro-optic effect in $BaTiO_3$ thin films [19]. Nevertheless, the relationship between the enhanced properties and quantum fluctuations remains largely unexplored.

Although epitaxial strain provides a powerful tuning knob to enhance the electro-optic response, strain relaxation limits the film thickness [20, 21], thereby constraining the degree of optical confinement for practical electro-optic devices [22]. These limitations motivate the development of alternative design strategies that create a large quantum-saturated electro-optic response without relying upon epitaxial strain.

In this work, we show how the conventional trade-off between the magnitude and thermal stability of the electro-optic response can be overcome by quantum fluctuations. Using phase-field simulations coupled with a thermodynamic analysis of optical properties, we first establish a direct relationship between the temperature-strain phase diagram and the electro-optic response in $BaTiO_3$. Quantum fluctuations of the ferroelectric soft mode are incorporated using a Barrett-type modification to the Landau coefficients [23], leading to a quantum-saturated electro-optic response over a moderate temperature window. Experimental measurements probe the saturation effect in $BaTiO_3$ thin films grown on $GdScO_3$ substrates, which are in quantitative agreement with the phase-field simulations and exceed the performance of previous $BaTiO_3$ thin films by a factor of 14 [13] and recent work on isotope-exchanged $SrTiO_3$ by a factor of 2.5 [24]. We further extend this design strategy to compositionally tuned $Ba_{1-x}Ca_xTiO_3$, which shows that a large quantum-saturated electro-optic response can be achieved without epitaxial strain. Together, these results establish a general design strategy to engineer high-performance electro-optic materials for quantum photonic technologies.

2 | Results

2.1 | Strain Tuning of the Electro-Optic Effect

Figure 1a presents the temperature-strain phase diagram of $BaTiO_3$ thin films. The phase at each point is largely determined by a combination of two thermodynamic driving forces: the intrinsic chemical stability of each ferroelectric phase, quantified by the Landau energy, and the elastic energy contribution, which favors phases closely matching the imposed strain. For a $BaTiO_3$ crystal in the absence of any applied stress/strain or electric field, the Landau energy determines the ranges of temperatures for the most stable ferroelectric state: the tetragonal phase ($P4mm$) from 400 to 270 K, the orthorhombic phase ($Amm2$) from 270 to 200 K and the rhombohedral phase ($R3m$) below 200 K [25]. The elastic energy, in contrast, biases the system toward phases or domain structures that best accommodate the imposed strain. A biaxial compressive strain promotes the ferroelectric phases or domain configurations that possess an out-of-plane component of the spontaneous polarization, such as the tetragonal *c*-phase. As the compressive strain increases, the tetragonal *c*-phase becomes increasingly favored, and beyond -1%, the 'as grown' phase diagram suggests that all ferroelectric–ferroelectric transitions are eliminated, leaving only the tetragonal *c*-phase (Figure 1a).

Strain can be leveraged to promote phase competition, creating regions of the phase diagram where multiple ferroelectric phases are nearly thermodynamically degenerate, resulting in a close energetic competition. In some cases, instead of forming a two-phase mixture, the system can resolve this phase competition by adopting an intermediate, lower-symmetry phase, that bridges between these two competing phases [26, 27]. Phase-field simulations reveal two distinct monoclinic phases (Figure 1a). The first is a monoclinic M_a phase (space group Cm), which acts as a bridge between the tetragonal and rhombohedral phases, marked by the orange region of the phase diagram, and the second is a monoclinic M_c phase (space group Pm), which acts as a bridge between the tetragonal and orthorhombic phases, marked by the pink region of the phase diagram. Figure 1b,c show the simulated r_{51} and r_{11} electro-optic response as a function of temperature and strain. Both the r_{51} and r_{11} electro-optic coefficients are maximized within the monoclinic M_c phase, with this enhancement becoming increasingly more pronounced as temperature decreases. While the monoclinic M_c phase has been observed in bulk $BaTiO_3$ in the vicinity of the tetragonal-to-orthorhombic phase transition [28–30], it is a metastable phase in the bulk and only exists within a narrow temperature range. By using epitaxial strain, this monoclinic phase can be thermodynamically stabilized over a broader region of the temperature-strain phase diagram, thus extending the window where the electro-optic response is enhanced. At low temperatures, quantum fluctuations of the ferroelectric soft mode suppress the temperature dependence of the ferroelectric phase boundaries leading to the temperature-independent electro-optic response [18].

Figure 2 focuses on the strain-dependent properties at 1 K, highlighting how the spontaneous polarizations and the lattice dielectric response govern the electro-optic coefficients. Figure 2a shows the strain dependence of the r_{11} and r_{51} electro-optic coefficients. Notably, these two coefficients reach their maximum value at two distinct strain states, with r_{11} peaking at -0.875% strain and r_{51} peaking at -0.925% strain. This behavior can be understood by examining the tensorial contributions to the electro-optic effect,

$$r_{ijk} \cong 2\epsilon_0 g_{ijmn} P^L_n \chi^L_{mk} \quad (1)$$

15214095, 0, Downloaded from https://advanced.onlinelibrary.wiley.com/doi/10.1002/adma.75543, Wiley Online Library on [16/11/2026]. See the Terms and Conditions (https://onlinelibrary.wiley.com/terms-and-conditions) on Wiley Online Library for rules of use; OA articles are governed by the applicable Creative Commons License

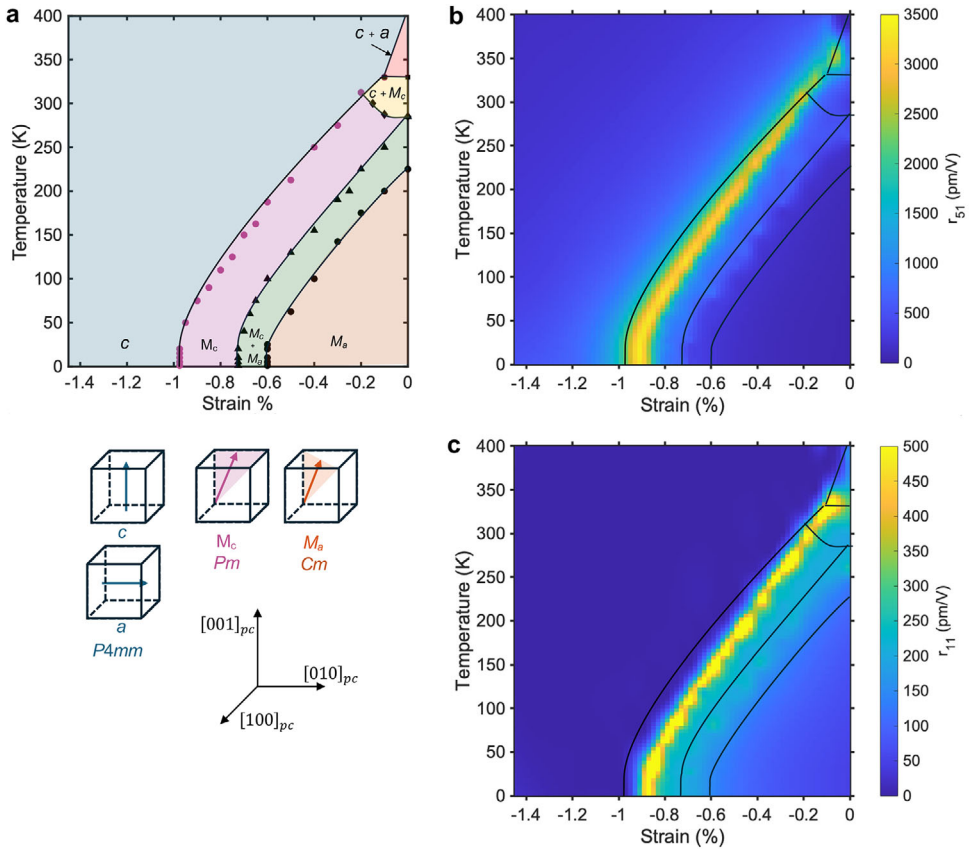


FIGURE 1 | Simulated strain-engineered electro-optic response of $BaTiO_3$. (a), Temperature-strain phase diagram of $BaTiO_3$ showing the stability regions of the tetragonal (*c* out-of-plane, *a* in-plane), monoclinic M_c and monoclinic M_a phases. (b,c) Temperature and strain dependence of the linear electro-optic r_{51} and r_{11}, respectively, for $BaTiO_3$, illustrating the relationship between the phase diagram and the electro-optic response.

where r_{ijk} is the electro-optic tensor, g_{ijkl} is the quadratic polar-optic tensor, P_i^L is the lattice polarization (the ionic and electronic contributions of the polarization that arises due to the displacement of the lattice) and χ_{ij}^L is the lattice dielectric susceptibility [11, 31].

For $BaTiO_3$, which possesses a cubic ($m\bar{3}m$) parent phase, and assuming the off-diagonal components of the dielectric tensor remain small, the expressions for the r_{11} (r_{111}) and r_{51}(r_{131}) electro-optic coefficients simplify to

$$r_{111} \cong 2\epsilon_0 g_{1111} P_1^L \chi_{11}^L \tag{2}$$

$$r_{131} \cong 2\epsilon_0 g_{1313} P_3^L \chi_{11}^L \tag{3}$$

where P_1^L and P_3^L are the in-plane and out-of-plane components of the lattice polarization, respectively, and χ_{11}^L is the in-plane lattice dielectric susceptibility. From Equations (2) and (3), the r_{11} requires a nonzero P_1^L and r_{51} electro-optic coefficient requires a nonzero P_3^L (Figure 2b). The χ_{11}^L lattice dielectric constant is maximized in the M_c phase at −0.925% strain, which coincides with the maximum for r_{51} since P_3^L remains nonzero across this region. Note that r_{11} peaks at a different strain value since it is dependent upon P_1^L, which is nearly 0 at -0.925% and increases with a decreasing strain. As a result, the product $P_1^L \chi_{11}^L$ is maximized at −0.875% rather than the strain where χ_{11}^L alone peaks, leading to distinct optimal conditions for r_{11} and r_{51}.

Figure 3 further examines the temperature dependence of the r_{51} and r_{11} electro-optic coefficients under different strain conditions and demonstrates the quantum saturation behavior. As shown in Figure 3a, the temperature at which r_{51} reaches its maximum shifts to lower values as the compressive strain increases from 0% to -1.2% strain. This trend coincides with the strain-dependent onset of the M_c phase reflected by the appearance of a nonzero r_{11} electro-optic coefficient, which is forbidden by symmetry in the tetragonal phase, but is allowed when the polarization rotates away from the tetragonal axis (Figure 3b). Beyond -1% compressive strain, the peak of the r_{51} coefficient shifts to 0 K and the magnitude of the r_{51} coefficient decreases with further compressive strain as the system moves away from this phase-competition region.

Across all strain conditions, the electro-optic coefficient becomes nearly temperature independent as $T \to 0$ K reflecting the quantum saturation of the electro-optic response [14]. At room temperature, thermal fluctuations dominate and the corresponding electro-optic properties strongly vary with temperature. Importantly, below a characteristic saturation temperature (T_s) quantum fluctuations become comparable to, or larger than thermal fluctuations leading to a temperature-independent electro-optic response [32]. Within a Landau mean-field treatment of the ferroelectric polarization, the fluctuations of the order parameter can be evaluated using either classical or quantum statistics [14, 18]. When these fluctuation amplitudes are inserted into the

15214095, 0, Downloaded from https://advanced.onlinelibrary.wiley.com/doi/10.1002/adma.75543, Wiley Online Library on [16/11/2026]. See the Terms and Conditions (https://onlinelibrary.wiley.com/terms-and-conditions) on Wiley Online Library for rules of use; OA articles are governed by the applicable Creative Commons License

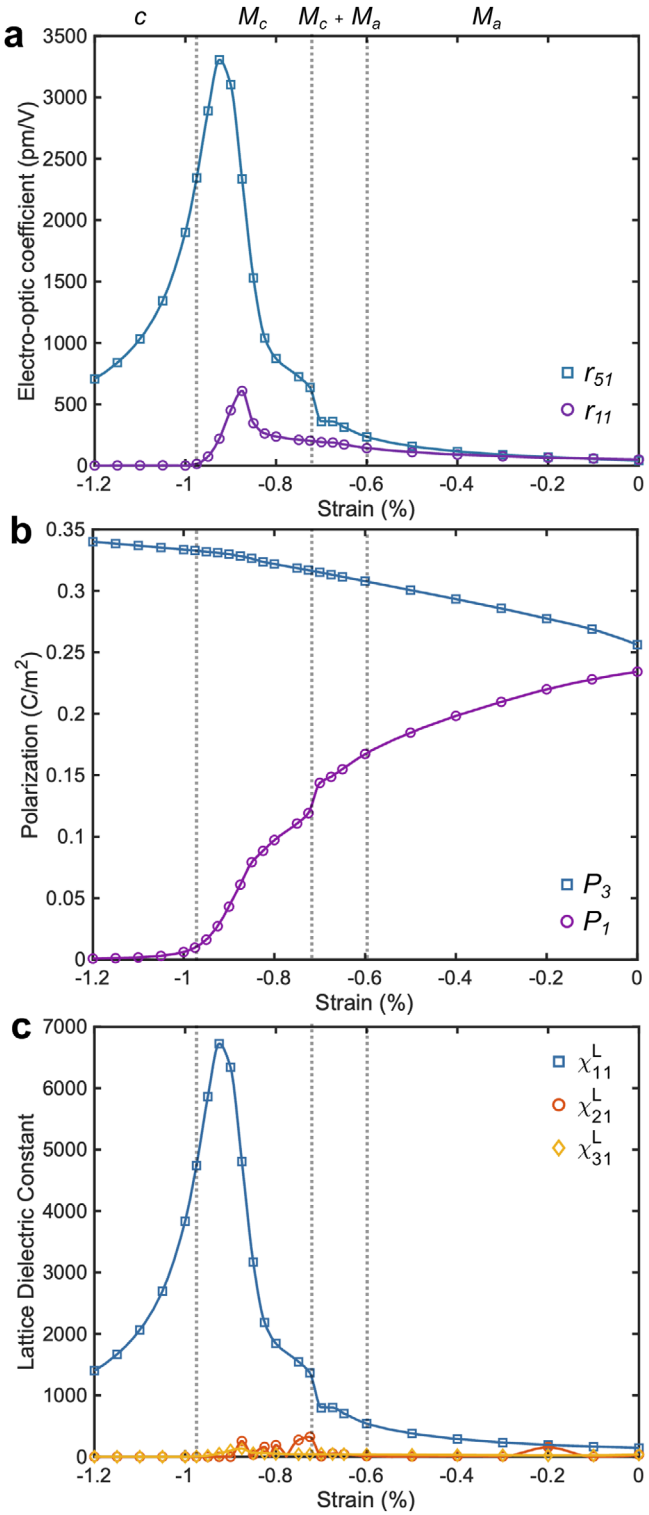


FIGURE 2 | Simulated strain-dependent electro-optic response, polarization and dielectric properties at 1 K. (a), spatially averaged linear electro-optic coefficients (r_{11} purple, r_{51} blue). (b), spontaneous polarization (P_1 purple, P_3 blue). (c), the lattice dielectric constants (χ^L_{11} blue, χ^L_{21} orange, χ^L_{31} yellow) at 1 K. The dashed lines indicate the phase boundaries. Symbols denote simulated data points, and the connecting lines are guides to the eye.

mean-field Landau expansion, e.g.,

$$f_{Landau} = a_1(T)\left(P_1^2 + P_2^2 + P_3^2\right) + a_{11}\left(P_1^4 + P_2^4 + P_3^4\right) + a_{12}\left(P_1^2P_2^2 + P_2^2P_3^2 + P_1^2P_3^2\right) + \cdots \quad (4)$$

the classical result (dashed black line) produces the typical Curie-Weiss form of the $a_1(T)$ coefficient

$$a_1(T) = a_0(T - T_c) \quad (5)$$

as shown by the dashed line in Figure 3c. In contrast, the quantum treatment requires a modification to the classical Curie-Weiss form. Their effect can be captured by introducing a quantum temperature scale where $T^Q = T_s \coth(\frac{T_s}{T})$ [32], $T^Q \approx T$ at high temperature and $T^Q \approx T_s$ as $T \to 0$ K. Substituting T^Q into the Curie-Weiss form yields a modified Curie-Weiss law called the Barrett function [23],

$$a_1(T) = a_0\left(T^Q - T_c^Q\right) = a_0\left(T_s \coth\left(\frac{T_s}{T}\right) - T_s \coth\left(\frac{T_s}{T_c}\right)\right) \quad (6)$$

which follows the classical expression at high temperatures, but exhibits low-temperature deviations due to quantum fluctuations (Figure 3c) [23]. When this quantum-corrected coefficient is used in the phase-field model, the calculated r_{51} electro-optic coefficient exhibits a pronounced plateau (Figure 3d solid line), in stark contrast to the peak near 40 K expected from a purely classical model (Figure 3d dashed line).

To experimentally realize this quantum-saturated electro-optic effect, $BaTiO_3$ films are epitaxially grown on $GdScO_3$ $(110)_O$ substrates, where the subscript O denotes orthorhombic indices, which impose a biaxial compressive strain of approximately $\varepsilon_{11} = -0.94\%$, $\varepsilon_{22} = -1.04\%$ at 293 K (see Figure S1 and Supplemental Note S3 and S4). Phase-field simulations predict a substantial increase of the electro-optic response with a saturation regime below 25 K, which agree with experimental measurements of the effective electro-optic coefficient (Figure 3e). The presence of the monoclinic phase is further supported by the observation of a spontaneous polarization component along the $[100]_{pc}$ direction, which is experimentally supported using second harmonic generation measurements (Figure 3f). The phase-field simulations predict that $BaTiO_3$ epitaxially strained on $GdScO_3$ possesses a single monoclinic C domain state below 75 K, therefore, the electro-optic effect describes the intrinsic single-domain behavior of the material.

2.2 | Chemical Tuning of the Electro-Optic Effect

While strain engineering is a powerful method for tuning the thermodynamic stability of different ferroelectric phases, it faces a fundamental limitation imposed by film thickness that may limit the potential scalability of strained films. In electro-optic devices, a key performance metric is the optical confinement factor, which quantifies the fraction of optical power guided within the electro-optic layer [22]. Thicker films increase the

15214095, 0, Downloaded from https://advanced.onlinelibrary.wiley.com/doi/10.1002/adma.75543, Wiley Online Library on [16/11/2026]. See the Terms and Conditions (https://onlinelibrary.wiley.com/terms-and-conditions) on Wiley Online Library for rules of use; OA articles are governed by the applicable Creative Commons License

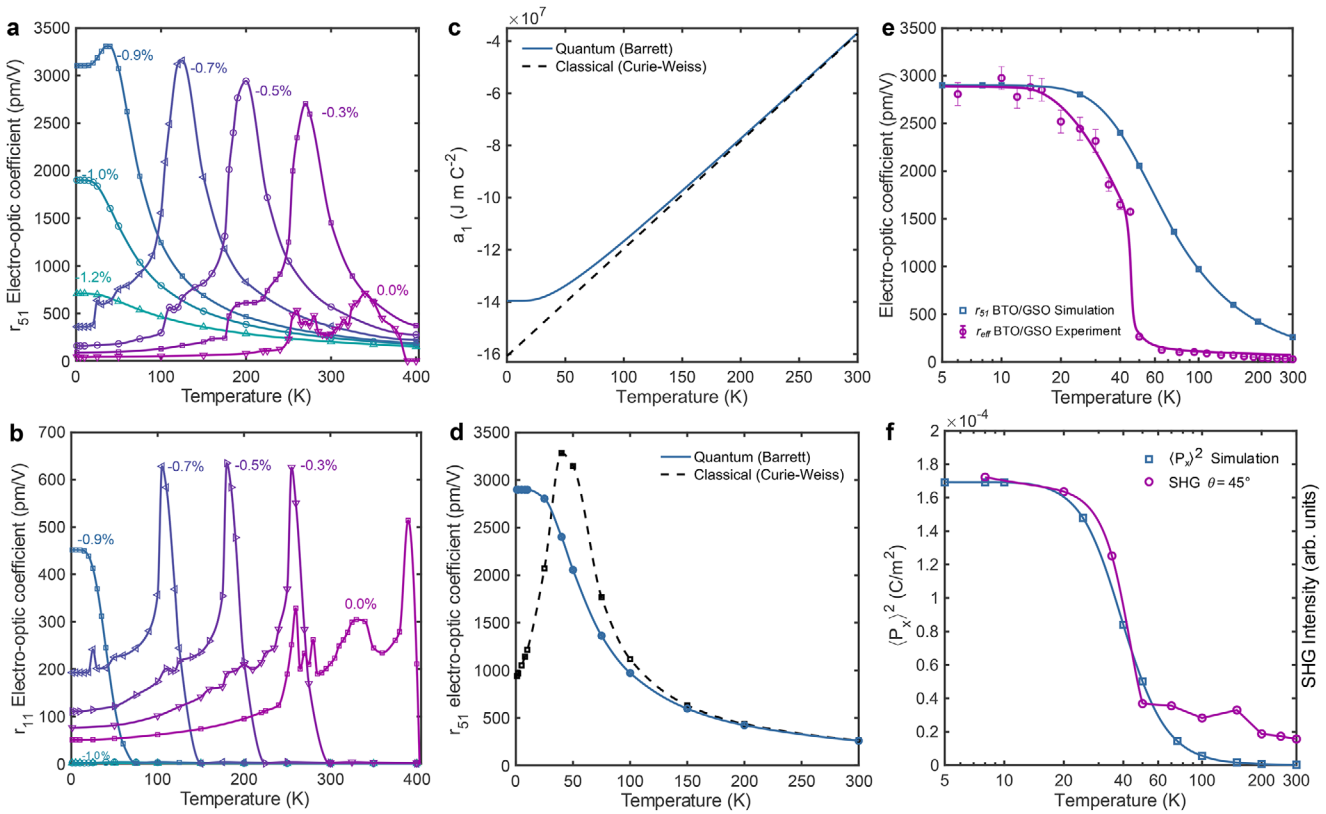


FIGURE 3 | Quantum saturation in the electro-optic effect. Simulated temperature dependence of the (a), r_{51} electro-optic coefficient and,(b) the r_{11} electro-optic coefficient. Increasing compressive strain shifts the maximum r_{51} and r_{11} to lower temperatures. (c) Simulated temperature dependence of the a_1 Landau coefficient assuming classical and quantum fluctuations. (d), Comparison of the simulated r_{51} electro-optic coefficient assuming classical and quantum fluctuations of $BaTiO_3$ epitaxially strained on $GdScO_3$. (e) Simulated and experimental electro-optic response of $BaTiO_3$ epitaxially strained on $GdScO_3$. (f), Tetragonal-to-monoclinic phase transition experimentally probed by second harmonic generation (SHG) [19], compared with the simulated mean-squared polarization along the $[100]_{pc}$ direction. Symbols denote simulated or experimental data points. In Panels a, b, d, e, and f, the connecting lines are guides to the eye. In panel c, the curves represent the theoretical temperature dependence of the Landau coefficient.

optical confinement, allowing for a larger fraction of the guided light to be actively modulated by the applied electric field. Unfortunately, the maximum film thickness is limited by the epitaxial strain, where beyond a critical thickness, strain relaxation occurs through the formation of dislocations [20, 21]. While this relaxation can be mitigated using superlattice architectures, it nevertheless introduces an inherent trade-off between strain tuning and optical confinement.

For example, using the Matthews-Blakeslee Criterion, when the misfit strain is between −0.8% and −0.9%, the critical thickness of $BaTiO_3$ is 5.9–6.8 nm, which represents a lower bound. Films can remain strained beyond the critical thickness because this criterion estimates the thickness at which a single threading dislocation is energetically favorable, but several dislocations must form to fully compensate the misfit strain and it does not consider the kinetic barriers for dislocation formation (see Supplemental Note S5).

Using the same design principle, one alternative strategy to mitigate this trade-off is to use composition as an additional tuning knob, offering a complementary pathway for optimizing cryogenic electro-optic materials. Importantly, compositional tuning does not impose a critical thickness enabling thicker electro-optic films with a large optical confinement factor.

Figure 4a presents the calculated temperature-composition diagram of $Ba_{1-x}Ca_xTiO_3$ under stress-free conditions, compared with experimentally determined phase boundaries [33, 34]. There are several examples of the growth of $Ba_{1-x}Ca_xTiO_3$ single crystals from $x = 0 - 0.3$, where beyond 0.3 mole fraction of $CaTiO_3$ the system has a two-phase mixture of barium-rich and calcium-rich regions [33–38]. Increasing the $CaTiO_3$ fraction progressively stabilizes the tetragonal phase at the expense of the orthorhombic and rhombohedral phases, shifting the phase boundaries to lower temperatures. Beyond 23% $CaTiO_3$ the phase diagram indicates that all ferroelectric–ferroelectric transitions are eliminated, leaving only the tetragonal phase (Figure 4a). The change in phase boundaries also changes the temperature at which the r_{51} electro-optic coefficient is calculated to be maximized (Figure 4b). As the concentration of $CaTiO_3$ is increased and the tetragonal-to-orthorhombic phase boundary is pushed to lower temperatures, the temperature where the r_{51} electro-optic coefficient is calculated to be maximized is also pushed to lower temperatures. At 23% $CaTiO_3$ the tetragonal-to-orthorhombic phase boundary is tuned to 0 K which maximizes the calculated r_{51}

15214095, 0, Downloaded from https://advanced.onlinelibrary.wiley.com/doi/10.1002/adma.75543, Wiley Online Library on [16/11/2026]. See the Terms and Conditions (https://onlinelibrary.wiley.com/terms-and-conditions) on Wiley Online Library for rules of use; OA articles are governed by the applicable Creative Commons License

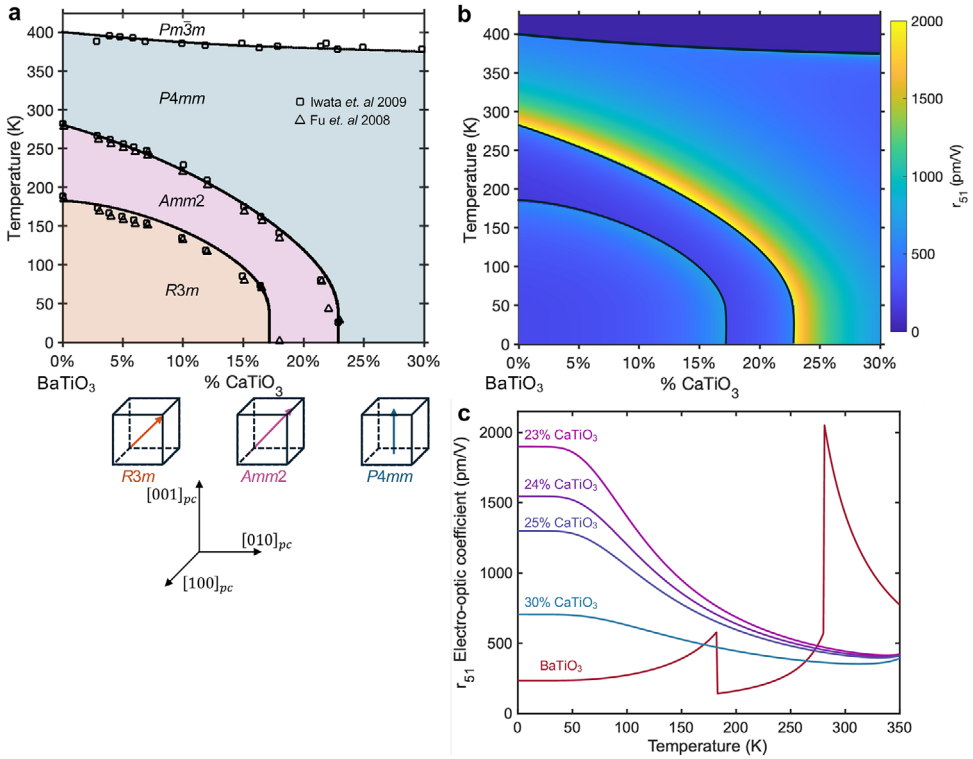


FIGURE 4 | Simulated chemically engineered electro-optic response in $Ba_{1-x}Ca_xTiO_3$. (a), Temperature-composition phase diagram of $Ba_{1-x}Ca_xTiO_3$ showing the stability regions of the tetragonal, orthorhombic, and rhombohedral phases. (b), Temperature and composition dependence of the calculated linear electro-optic r_{51} for $Ba_{1-x}Ca_xTiO_3$ illustrating the relationship between the phase diagram and the electro-optic response. (c), Calculated temperature dependence of the r_{51} electro-optic coefficient under different $CaTiO_3$ concentrations.

electro-optic coefficient directly within the quantum saturation regime. Notably, the material congruently melts at $Ba_{0.77}Ca_{0.23}TiO_3$ which also aligns with the maximum cryogenic electro-optic effect [35–37]. Beyond 23% $CaTiO_3$, the maximum calculated r_{51} coefficient shifts to 0 K and the magnitude of the calculated r_{51} coefficient decreases as the $CaTiO_3$ concentration is further increased (Figure 4c).

2.3 | Electro-Optic Performance in the Quantum Saturation Regime

Figure 5 compares the temperature-dependent electro-optic coefficients of several representative materials, including strained $BaTiO_3$ on $GdScO_3$ (this work), $Ba_{0.77}Ca_{0.23}TiO_3$ (this work), bulk $BaTiO_3$ [10, 11], $BaTiO_3$ on Si [13], electrically biased $SrTiO_3$ and electrically biased SrTi $(O^{16}_{0.67}O^{18}_{0.33})_3$ [24]. In the high-temperature regime, large electro-optic coefficients are typically confined to a narrow temperature window, with small changes in temperature causing large changes in the electro-optic response, as seen in the behavior of the r_{51} coefficient of bulk $BaTiO_3$ near room temperature [10, 11]. In contrast, in the quantum-saturated regime, a large electro-optic coefficient can be combined with a small thermal sensitivity so the response varies only weakly over a broad temperature range, as observed in the behavior of $BaTiO_3$ on $GdScO_3$, $Ba_{0.77}Ca_{0.23}TiO_3$, electrically biased $SrTiO_3$ and electrically biased SrTi $(O^{16}_{0.67}O^{18}_{0.33})_3$ [24]. This illustrates that quantum saturation can overcome the usual trade-off between magnitude and thermal sensitivity. Notably, the cryogenic electro-optic response of $BaTiO_3$ on $GdScO_3$ is comparable to the peak electro-optic effect observed in bulk $BaTiO_3$ near room temperature. Moreover, the electro-optic coefficient is approximately 14 times larger than the cryogenic electro-optic coefficient measured in $BaTiO_3$ on Si and about 2.5 times larger than recent reports of electrically biased SrTi $(O^{16}_{0.67}O^{18}_{0.33})_3$ [13, 24].

3 | Discussion

In this work, we demonstrate that the conventional trade-off between large electro-optic responses and thermal stability can be overcome by harnessing quantum fluctuations in ferroelectric materials. By tuning the ferroelectric phase boundaries to 0 K using strain or composition, we engineer a cryogenic electro-optic response that is over an order of magnitude larger than strain-relaxed $BaTiO_3$. The combination of a large low-temperature electro-optic coefficient and a small thermal sensitivity demonstrates that strain/composition engineering and quantum saturation can be used to create high-performance electro-optic materials for quantum technologies. We demonstrate that this design principle is not limited to epitaxially strained thin films and show that compositional tuning in $Ba_{1-x}Ca_xTiO_3$ offers a complementary route toward large cryogenic electro-optic properties which can be readily implemented in established commercial synthesis techniques, without the need of rare isotopes as required in isotope-substituted SrTi $(O^{16}_{0.67}O^{18}_{0.33})_3$ [24].

Importantly, we find that merely stabilizing the tetragonal phase of $BaTiO_3$ is insufficient to sustain a large electro-optic coefficient at cryogenic temperatures, despite what may be inferred from the

15214095, 0, Downloaded from https://advanced.onlinelibrary.wiley.com/doi/10.1002/adma.75543, Wiley Online Library on [16/11/2026]. See the Terms and Conditions (https://onlinelibrary.wiley.com/terms-and-conditions) on Wiley Online Library for rules of use; OA articles are governed by the applicable Creative Commons License

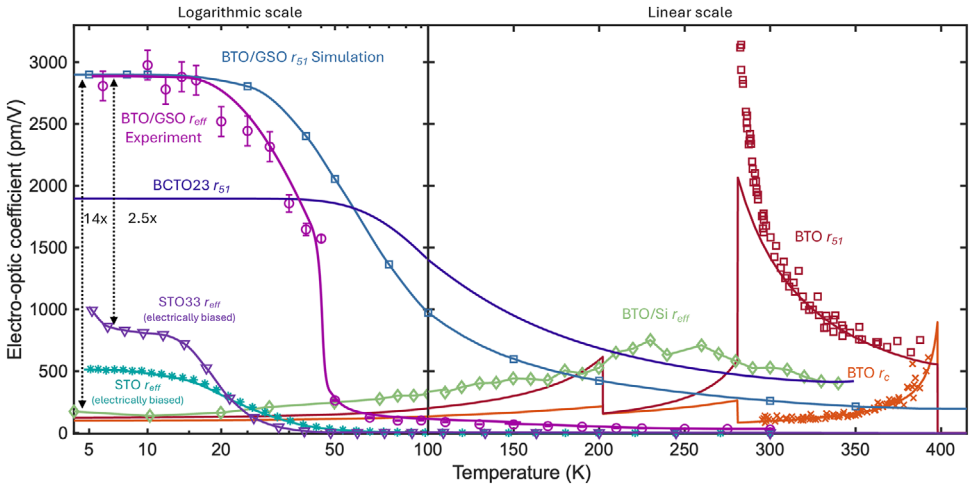


FIGURE 5 | Temperature-dependent electro-optic coefficients across different material platforms. Temperature dependence of the linear electro-optic coefficient for bulk $BaTiO_3$ (BTO) (squares: experiment [10], solid line: theory [11]), $Ba_{0.77}Ca_{0.23}TiO_3$ (BCTO23) (theory), $BaTiO_3$ on Si (BTO/Si) [13] (experiment), electrically biased $SrTiO_3$ (STO) (experiment), and isotope-substituted SrTi $(O^{16}_{0.67}O^{18}_{0.33})_3$ (STO33) [24] (experiment) and $BaTiO_3$ on $GdScO_3$ (BTO/GSO) (circles: experiment, squares: theory, the solid line denotes a guide to the eye).

room temperature behavior. While the tetragonal phase exhibits a large electro-optic response at room temperature, this enhancement primarily arises from its proximity to the tetragonal-to-orthorhombic phase boundary. Our findings underscore the importance of engineering phase competition to achieve large electro-optic effects. Although this current work takes advantage of quantum effects to stabilize phase competition over a broad temperature range, the underlying design principle promoting phase competition offers a broadly applicable framework for developing high-performance electro-optic materials across a wide range of temperatures.

Although currently these quantum effects are confined to the cryogenic regime, in principle these effects could be pushed to higher temperatures. In $BaTiO_3$, the saturation temperature (T_s) is set by the characteristic energy of the ferroelectric soft mode, but in principle, by changing the chemical composition or coupling to other lattice modes, this saturation temperature could be shifted to higher temperatures. This is analogous to the heat capacity of diamond near room temperature [39], where the high characteristic phonon energy pushes the onset of classical behavior to high temperatures. By analogy, designing ferroelectrics with higher-frequency soft modes or engineering the coupling between other modes could raise the saturation temperature, opening the possibility of a room-temperature quantum-saturated electro-optic response [40].

The design strategy demonstrated here is not limited to $BaTiO_3$ or $Ba_{1-x}Ca_xTiO_3$ and extending the present analysis to other material systems could identify material platforms that can produce large cryogenic electro-optic responses. Moreover, these findings are not limited to the electro-optic effect and may be extended to other properties such as the piezoelectric or piezo-optic effect. In this sense, $BaTiO_3$ strained to $GdScO_3$ and $Ba_{1-x}Ca_xTiO_3$ serve as model systems illustrating how phase competition and quantum fluctuations can be deliberately engineered to enable a high-performance electro-optic response.

4 | Conclusion

We demonstrate that quantum fluctuations in ferroelectric materials can overcome the conventional trade-off between the magnitude and thermal sensitivity of the electro-optic response. By tuning the ferroelectric phase boundaries down to 0 K through either epitaxial strain or chemical composition, we engineer an electro-optic response that exceeds $BaTiO_3$ on Si by an order of magnitude while remaining insensitive to temperature below 25 K. Notably, $Ba_{1-x}Ca_xTiO_3$ enables electro-optic thin films with a large optical confinement which are compatible with established commercial synthesis methods. Although the quantum saturated regime explored here is confined to cryogenic temperatures, extending this framework to materials with higher-energy soft modes or tailored lattice couplings offers a compelling pathway to raise the saturation temperature. More broadly, this general design strategy is not limited to the electro-optic effect and may be an effective design strategy to enhance piezoelectric and piezo-optic responses to support a broad range of cryogenic quantum technologies.

5 | Methods

5.1 | Phase-Field Simulations

Based on the thermodynamic theory of optical properties, we may formulate a phase-field model, where the thermodynamics of the ferroelectric system is described by its free energy functional,

$$F = \int \left[f^L\left(T, P_i^L\right) + f^e\left(T, P_i^e\right) + f^{L-e}\left(P_i^L, P_i^e\right) + f^{grad}\left(\nabla_i P_j^L\right) + f^{elas}\left(P_i^L, P_i^e, \varepsilon_{ij}\right) + f^{elec}\left(P_i^L, P_i^e, E_i\right)\right] dx^3 \quad (7)$$

where $P_i^L(x_i, t)$ is the lattice polarization, $P_i^e(x_i, t)$ is the electronic polarization and $\varepsilon_{ij}(x_i, t)$ is the strain [11].

15214095, 0, Downloaded from https://advanced.onlinelibrary.wiley.com/doi/10.1002/adma.75543, Wiley Online Library on [16/11/2026]. See the Terms and Conditions (https://onlinelibrary.wiley.com/terms-and-conditions) on Wiley Online Library for rules of use; OA articles are governed by the applicable Creative Commons License

The respective evolution of the lattice polarization and electronic polarization is solved separately. The lattice polarization is computed following the relaxational approximation, where we assume relaxational kinetics for the lattice polarization, and the mechanical displacement, electrical potential, and electrical polarization instantaneously reach equilibrium, leading to the time-dependent Ginzburg-Landau equation

$$\gamma_{ij}^{L}\frac{\partial P_{j}^{L}}{\partial t}=-\frac{\delta F}{\delta P_{i}^{L}} \tag{8}$$

where $-\frac{\delta F}{\delta P_i^L}$ is the thermodynamic driving force for the temporal evolution of the lattice polarization. We use the local stress and lattice polarization distribution as inputs to the electronic polarization dynamic equation

$$\mu_{ij}^{e}\frac{\partial^{2}P_{j}^{e}}{\partial t^{2}}+\gamma_{ij}^{e}\frac{\partial P_{j}^{e}}{\partial t}=-\frac{\delta F}{\delta P_{i}^{e}} \tag{9}$$

where $-\frac{\delta F}{\delta P_i^e}$ is the thermodynamic driving force for the temporal evolution of the electronic polarization. To compute the local electronic dielectric susceptibility, we solve Equation (9) assuming a small periodic electric field is applied, which yields an analytical solution

$$\chi_{ij}^{e,1}\left(x_{i},\omega\right)=\left[B_{ij}^{e}\left(x_{i}\right)-\epsilon_{0}\left(i\omega\gamma_{ij}^{e}+\omega^{2}\mu_{ij}^{e}\right)\right]^{-1} \tag{10}$$

which is related to the curvature of the free-energy landscape with respect to the electronic polarization by, $B_{ij}^{e}(x_i)=\varepsilon_0(\frac{\partial^2 f}{\partial P_i^e,\partial P_j^e})$. Solving Equation (10) (assuming $\lambda = 1550\ nm$) we may compute the local refractive indices from the local lattice polarization and stress distribution, thereby naturally including the electro-optic effect and potential piezo-optic effects. As the lattice polarization distribution evolves in response to an applied electric field, the corresponding change to the electronic dielectric susceptibility and the refractive index is computed.

Here $f^{L}(P_i^L)$ describes the intrinsic stability of the lattice polarization compared to the high-symmetry phase ($m\bar{3}m$) as a Taylor expansion of the polarization about the high-symmetry phase, this is equivalent to the Landau free energy density:

$$\begin{aligned}f^{L}\left(T,\,P_{i}^{L}\right)=f_{o}+a_{ij}\left(T\right)P_{i}^{L}P_{j}^{L}+a_{ijkl}P_{i}^{L}P_{j}^{L}P_{k}^{L}P_{l}^{L}\\+a_{ijklmn}P_{i}^{L}P_{j}^{L}P_{k}^{L}P_{l}^{L}P_{m}^{L}P_{n}^{L}+a_{ijklmnop}P_{i}^{L}P_{j}^{L}P_{k}^{L}P_{l}^{L}P_{m}^{L}P_{n}^{L}P_{o}^{L}P_{p}^{L}\end{aligned} \tag{11}$$

where a_{ij}, a_{ijkl}, a_{ijklmn}, and $a_{ijklmnop}$ are the dielectric stiffness coefficients measured under constant stress conditions. For $BaTiO_3$, an eighth-order expansion is used to describe the stability of the lattice polarization. The thermodynamic coefficients are adapted from ref. [25] to describe the effects of quantum fluctuations at cryogenic temperatures [23].

The intrinsic free energy density of the electronic polarization, in the absence of the lattice polarization, is described by

$$f^{e}\left(T,P_{i}^{e}\right)=\frac{1}{2\epsilon_{0}}B_{ij}^{e,ref}\left(T\right)P_{i}^{e}P_{j}^{e} \tag{12}$$

where $B_{ij}^{e,ref}(T)$ is related to the refractive index of the equivalent high-symmetry phase. The coupling energy density between the lattice and electronic polarization, which determines the electro-optic effect is given by

$$f^{L-e}\left(P_{j}^{L},P_{i}^{e}\right)=\frac{1}{2\epsilon_{0}}g_{ijkl}^{LL}P_{l}^{L}P_{k}^{L}P_{i}^{e}P_{j}^{e} \tag{13}$$

where g_{ijkl}^{LL} relates the lattice polarization to the refractive index.

The gradient energy density is represented by

$$f_{grad}=\frac{1}{2}\,G_{ijkl}\frac{\partial P_{i}^{L}}{\partial x_{j}}\frac{\partial P_{k}^{L}}{\partial x_{l}} \tag{14}$$

where G_{ijkl} is the gradient energy tensor where the nonzero coefficients are chosen to be $G_{11} = 0.6$, $G_{12} = -0.6$ and $G_{44} = 0.6$, and the units are normalized by $a_1 l_o^2$, where a_1 is the first Landau expansion coefficient and l_o is chosen as 1 nm per grid point.

The elastic energy is given by

$$f^{elas}\ \left(P_{i}^{L},\,P_{i}^{e},\,\varepsilon_{ij}\right)=\frac{1}{2}\,C_{ijkl}\left(\varepsilon_{ij}-\varepsilon_{ij}^{o}\right)\left(\varepsilon_{kl}-\varepsilon_{kl}^{o}\right) \tag{15}$$

where C_{ijkl} is the elastic stiffness, ε_{ij} is the total strain, and $\varepsilon_{ij}^{o}=Q_{ijkl}P_{k}^{L}P_{l}^{L}+\frac{1}{2\epsilon_{0}}\pi_{ijkl}P_{k}^{e}P_{l}^{e}$ is the eigenstrain, where Q_{ijkl} is the electrostrictive coefficient and π_{ijkl} is the piezo-optic tensor for the high-symmetry phase. The total strain is solved for a thin film boundary condition assuming that the strain relaxes to its equilibrium value at each time step; for simplicity, we ignore the contribution of the electronic polarization to the eigenstrain. Further details on solving the elasticity may be found in Ref. [41].

The electrostatic energy is given by

$$f^{elec}=-E_{i}P_{i}^{L}-E_{i}P_{i}^{e}-\frac{1}{2}\epsilon_{0}k_{ij}^{b}E_{i}E_{j} \tag{16}$$

where ϵ_0 is the vacuum permittivity and κ_{ij}^{b} is the background dielectric constant. For simplicity, to compute evolution of the lattice polarization, we only include the linear contribution to electronic polarization and add it to the background dielectric constant yielding $f^{elec}=-E_{i}P_{i}^{L}-\frac{1}{2}\epsilon_{0}\kappa_{ij}^{b}E_{i}E_{j}$, where $\kappa_{ij}^{b}=10$ and is isotropic. Here κ_{ij}^{b} contains contributions from the electronic contribution and the vacuum and other hard modes. A table containing all coefficients used in the phase-field simulations is given in the supplementary material (Table S1).

For the simulations, a system size of $128\ \Delta x_1 \times 128\ \Delta x_2\ \times 36\ \Delta x_3$ is used. There are $12\ \Delta x_3$ grid points for the substrate where the elastic constants are assumed to be the same as the ferroelectric film, and there are $4\ \Delta x_3$ grid points acting as an air layer above the film. The thickness of $BaTiO_3$ is set to be $20\ \Delta x_3$. Periodic boundary conditions are used along the in-plane lateral directions, and natural boundary conditions are used along the film-substrate and film-air interfaces. The interface between the film and the substrate is assumed to be coherent, and hence the misfit strain is calculated using the equivalent cubic lattice parameters for $BaTiO_3$ and the pseudocubic lattice parameters for

15214095, 0, Downloaded from https://advanced.onlinelibrary.wiley.com/doi/10.1002/adma.75543, Wiley Online Library on [16/11/2026]. See the Terms and Conditions (https://onlinelibrary.wiley.com/terms-and-conditions) on Wiley Online Library for rules of use; OA articles are governed by the applicable Creative Commons License

$GdScO_3$ [42].

$$\varepsilon_{11} = \frac{a^{[110]_o}_{GdScO3} - a^{eq}_{BaTiO3}}{a^{eq}_{BaTiO3}}, \ \varepsilon_{22} = \frac{a^{[001]_o}_{GdScO3} - a^{eq}_{BaTiO3}}{a^{eq}_{BaTiO3}} \ \varepsilon_{12} = \varepsilon_{21} = 0 \tag{17}$$

where the lattice parameters for $BaTiO_3$ are $a^{eq}_{BaTiO3} = 4.008\ \text{Å}\ (1 + 1.15 \times 10^{-5}(T - 300\ \text{K}))$ and $GdScO_3$ are $a^{[110]_O}_{GdScO3} = 3.970\ \text{Å}\ (1 + 1.09 \times 10^{-5}(T - 300\ \text{K}))$ and $a^{[001]_o}_{GdScO3} = 3.966\ \text{Å}\ (1 + 1.09 \times 10^{-5}(T - 300\ \text{K}))$.

The simulations begin with an initial condition of $P^L_i\ (x_i,\ t = 0) = [0.0\ 0.0\ 0.1\ \text{C m}^{-2}] + \Delta P^{noise}(x_i,\ t = 0)$, where $|P^{noise}| = 0.1\ \text{C m}^{-2}$, and relax for 20,000 time steps. To simulate the evolution of the polarization under an applied electric field and the corresponding electro-optic effect, a uniform electric field is applied along the $[100]_{pc}$ direction ranging from -70 kV cm^{-1} to 70 kV cm^{-1}, which varies in time with a sine wave, with one period being equal to 65,000 time steps. The linear electro-optic effect is found by taking the average of the refractive index over the ferroelectric material as a function of an applied electric field and fitting to a cubic polynomial centered at zero electric field. We note that the phase-field results reported here exhibit quantitative differences from our earlier work [19]. These discrepancies arise primarily from the use of a larger simulation domain and a slower electric-field ramp rate, choices made to more faithfully reproduce the experimental conditions. The lattice–polarization evolution was computed using the MuPRO phase-field simulation package [43].

5.2 | Thermodynamic Analysis

Using the thermodynamic energy density function in Equation (7), we evaluate the ferroelectric and optical properties of $Ba_{1-x}Ca_xTiO_3$ assuming a single-domain state under stress-free conditions. First, the equilibrium lattice and electronic polarizations are found by solving the following coupled equations

$$\left(\frac{\partial f}{\partial P^L_i}\right)_{T,\ \sigma,\ P^e} = 0, \ \left(\frac{\partial f}{\partial P^e_i}\right)_{T,\ \sigma,\ P^L} = 0 \tag{18}$$

Under zero applied electric field, the electronic polarization by definition will be equal to zero [11].

The lattice dielectric susceptibility is then given by

$$\chi^L_{ij} = \frac{1}{\epsilon_0}\left(\frac{\partial P^L_i}{\partial E_j}\right)_{T,\ \sigma} = \frac{1}{\epsilon_0}\left(\frac{\partial^2 f}{\partial P^L_i \partial P^L_j}\right)^{-1}_{T,\sigma} \tag{19}$$

To account for optical dispersion and loss, we can utilize the polarization equation of motion

$$\mu^e_{ij}\frac{\partial^2 P^e_j}{\partial t^2} + \gamma^e_{ij}\frac{\partial P^e_j}{\partial t} = -\frac{\delta F}{\delta P^e_i} \tag{20}$$

where μ^e_{ij} is the electronic polarization effective mass and γ^e_{ij} is the electronic polarization damping coefficient. Solving Equation (20) using a perturbation expansion yields

$$\chi^e_{ij} = n^2 - \delta_{ij} = \left[B^e_{ij} - \epsilon_0\left(i\omega\gamma^e_{ij} + \omega^2\mu^e_{ij}\right)\right]^{-1} \tag{21}$$

where n is the refractive index and $B^e_{ij} = \epsilon_0\left(\frac{\partial^2 f}{\partial P^e_i \partial P^e_j}\right)_{T,\ \sigma}$ is the electronic dielectric stiffness. Which can be used to calculate the optical frequency dependence of the electro-optic effect via

$$r^L_{ijk}(\omega) = \left(\frac{\partial B_{ij}(\omega)}{\partial P^L_m}\right)_{T,\ \sigma}\left(\frac{\partial P^L_m}{\partial E_k}\right)_{T,\ \sigma} = \epsilon_0 f^L_{ijm}(\omega)\,\chi^L_{mk} \tag{22}$$

where,

$$f^L_{ijk} = \left(\frac{\partial B_{ij}(\omega)}{\partial P^L_k}\right)_{T,\sigma} = \left(\frac{\partial B_{ij}(\omega)}{\partial B^e_{mn}}\right)_{T,\sigma}\left(\frac{\partial B^e_{mn}}{\partial P^L_k}\right)_{T,\sigma} = \left(\frac{\partial B_{ij}(\omega)}{\partial B^e_{mn}}\right)_{T,\sigma}\left(\frac{\partial^3 f}{\partial P^e_m \partial P^e_n \partial P^L_k}\right)_{T,\sigma}$$
$$= \left[\left(B^e - \epsilon_0\omega^2\mu^e + \mathbb{I}\right)^{-1}\right]_{mi}\left[\left(B^e - \epsilon_0\omega^2\mu^e + \mathbb{I}\right)^{-1}\right]_{nj}\left[2g^{LL}_{mnkl}P^L_l + g^{Le}_{mnkl}P^e_l\right] \tag{23}$$

In all calculations, we find the frequency ω assuming $\lambda = 1550\ nm$. The thermodynamic coefficients for $Ba_{1-x}Ca_xTiO_3$ are given in Table S2 and were fit to experimental measurements of the spontaneous polarization, phase transition temperatures and dielectric constants [33, 34, 44, 45]. For simplicity, we ignore the composition dependence of the quadratic polar-optic tensor, and reference electronic dielectric stiffness and use the values obtained for $BaTiO_3$.

5.3 | Growth of $BaTiO_3$ on $GdScO_3$ Thin Films

The sample was grown in a Veeco GEN10 MBE system equipped with an Epiray GmbH THERMALAS laser substrate heater, which is a 1 kW CO_2 laser with a wavelength of 10.6 μm that irradiates the backside of the substrate over a circular area with a diameter of approximately 14 mm. Barium (Sigma-Aldrich, 99.99% purity) was supplied using a conventional differentially pumped effusion cell and titanium using a Veeco Ti-Ball source. The sources were simply co-deposited. The barium flux was approximately 5×10^{13} atoms/($cm^2 \times s$) and the titanium flux was approximately 1×10^{13} atoms/($cm^2 \times s$), creating a Ba:Ti flux ratio of 5:1. The barium flux was determined by a quartz crystal microbalance, and the titanium flux by x-ray reflectivity of a calibration film of $BaTiO_3$ grown on an $SrTiO_3$ (001) substrate at $T_{sub} = 1200°C$, with an oxidant pressure of 1×10^{-6} Torr of O_2 + 10% O_3 and a Ba:Ti ratio of 5:1. The $BaTiO_3$ film was grown on a $GdScO_3$ $(110)_O$ substrate (CrysTec GmbH), to a thickness of approximately 36 nm.

Ozone was used as the oxidant at a background pressure of $1{\times}10^{-6}$ Torr of O_2 + 10% O_3. The film was cooled in the same oxidant and pressure in which it was grown to $T_{sub} < 200°C$ before the oxidant was turned off. The substrate temperature, measured by a pyrometer operating at 7.5 μm on the backside of the substrate during growth, was 1160°C. Due to the high substrate temperature, the vapor pressure of barium-containing species over $BaTiO_3$, chiefly BaO, is significantly higher than that of titanium-containing species over $BaTiO_3$, so excess barium will desorb from the surface leaving behind a single-phase $BaTiO_3$ film within an adsorption-controlled growth window. As $GdScO_3$

15214095, 0, Downloaded from https://advanced.onlinelibrary.wiley.com/doi/10.1002/adma.75543, Wiley Online Library on [16/11/2026]. See the Terms and Conditions (https://onlinelibrary.wiley.com/terms-and-conditions) on Wiley Online Library for rules of use; OA articles are governed by the applicable Creative Commons License

absorbs well at 10.6 μm, the backside of the substrate was not coated.

X-ray diffraction (XRD) and reciprocal space mapping (RSM) analysis was done with a Panalytical Empyrean x-ray diffractometer using Cu $K_{\alpha 1}$ radiation. Atomic force microscopy (AFM) was done using an Asylum Cypher ES Environmental AFM. RHEED images were taken during growth using a Staib electron source operating at 14 kV.

5.4 | Polarization-Based Electro-Optic Measurement

Electro-optic measurements were performed using a home-built polarizer-sample-compensator-analyzer PSCA setup with a 1550 nm HP 81689A continuous-wave laser source and a Nirvana 2017 balanced detector (Figure S2). For absolute intensity measurements, a mechanical chopper was placed in the laser path and modulated at 1.54 kHz for detection with a Stanford SR830 lock-in amplifier. For measuring the modulated transmission intensity, an Agilent 33220A signal generator amplified by a Trek 610C high-voltage amplifier was used to apply a 555 Hz sine wave to the sample with the lock-in amplifier reference signal changed to the function generator reference. Samples were cooled to liquid He temperatures using a Janis 30 continuous flow cryostat system. To assess the frequency dependence of the electro-optic response, additional measurements were performed over modulation frequencies ranging from 555 Hz to 100 kHz. We observe a minimal change of the electro-optic effect within the measured frequency range, where the electro-optic coefficient remains within ± 6% of the observed values (see Supplemental Note S7 and Figure S5).

The polarization of the probe is set to lie between the ordinary and extraordinary refractive indices. An analyzer placed at the end of the setup is oriented orthogonal to the initial probe polarization state, resulting in no transmission of light through the setup when the sample and compensator are not included. With the sample introduced, the transmission becomes nonzero on account of the birefringence-induced ellipticity. A quarter-wave compensator is then added immediately after the sample to cancel out the native material birefringence with no voltage applied. This returns the transmission of the setup to zero until a voltage is applied to modulate the sample refractive indices and reintroduce ellipticity to the probe. Further details regarding the electro-optic measurements are provided in Supplemental Note S6 and Figures S2–S4.

5.5 | Second-Harmonic Generation Polarimetry

Second-harmonic generation polarimetry experiments were performed using a fundamental wavelength of 800 nm generated by a Spectra-Physics Solstice Ace amplified Ti:Sapphire laser with a 1 kHz repetition rate and 100 fs pulse width. Light was focused onto the sample using a 10 cm focal length lens, producing a 50 μm diameter spot size as determined by knife-edge measurements. Samples were cooled to liquid He temperatures using a Janis 30 continuous flow cryostat system. A bare $GdScO_3$ $(110)_O$ substrate of the same type produces no appreciable SHG signal under the same incident power, and thus the SHG signal measured is interpreted as originating entirely from the strained $BaTiO_3$ film.

Author Contributions

Aiden Ross: conceptualization, methodology, software, data curation, investigation, formal analysis, visualization, writing – original draft. **Sankalpa Hazra**: investigation, formal analysis, writing – review and editing, validation. **Albert Suceava**: investigation, formal analysis, writing – review and editing, validation. **Dylan Sotir**: investigation, formal analysis, writing – review and editing. **Ian Reed Philippi**: investigation, validation, formal analysis, writing – review and editing. **Darrell G. Schlom**: resources, supervision, writing – review and editing, funding acquisition. **Venkatraman Gopalan**: supervision, funding acquisition, resources, writing – review and editing. **Long-Qing Chen**: supervision, funding acquisition, resources, writing – original draft.

Acknowledgements

The work was primarily supported by the National Science Foundation under award number DMR-2522897. A.R. and I.R.P. acknowledge the support of the National Science Foundation Graduate Research Fellowship Program under Grant no. DGE1255832. The phase-field simulations in this work were performed using Bridges-2 at the Pittsburgh Supercomputing Center through allocation MAT230041 from the ACCESS program, which is supported by National Science Foundation grants #2138259, #2138286, #2138307, #2137603, and #2138296. The $BaTiO_3$ thin films were synthesized at the Platform for the Accelerated Realization, Analysis, and Discovery of Interface Materials (PARADIM), which is supported by the National Science Foundation (NSF) under Cooperative Agreement No. DMR-2039380. D.S. and D.G.S. acknowledge support from the NSF through PARADIM under Cooperative Agreement No. DMR-2039380.

Funding

National Science Foundation under award number DMR-2522897. National Science Foundation Graduate Research Fellowship Program under Grant no. DGE1255832. National Science Foundation (NSF) under Cooperative Agreement No. DMR-2039380.

Conflicts of Interest

The authors have a provisional patent filed on this work. Long-Qing Chen has a financial interest in MuPRO, LLC, a company which licenses and markets the software package used in this research.

Data Availability Statement

The data that support the findings of this study are available within the article. Datasets used for the generation of the figures and simulation input files are available at https://doi.org/10.5281/zenodo.17842835. Additional information relating to the film growth and structural characterization is available at https://doi.org/10.34863/k6vg-fr77. The MuPRO code package used in this work to carry out the phase-field simulation can be obtained after a user license is authorized by the MuPRO Company (https://mupro.co/). Any additional data connected to the study are available from the corresponding author upon reasonable request.

References

1. S. Krinner, S. Storz, P. Kurpiers, et al., "Engineering Cryogenic Setups for 100-qubit Scale Superconducting Circuit Systems," *EPJ Quantum Technology* 6 (2019): 2, https://doi.org/10.1140/epjqt/s40507-019-0072-0.

2. S. Krastanov, H. Raniwala, J. Holzgrafe, et al., "Optically Heralded Entanglement of Superconducting Systems in Quantum Networks," *Physical Review Letters* 127 (2021): 040503, https://doi.org/10.1103/PhysRevLett.127.040503.

15214095, 0, Downloaded from https://advanced.onlinelibrary.wiley.com/doi/10.1002/adma.75543, Wiley Online Library on [16/11/2026]. See the Terms and Conditions (https://onlinelibrary.wiley.com/terms-and-conditions) on Wiley Online Library for rules of use; OA articles are governed by the applicable Creative Commons License

3. F. Lecocq, F. Quinlan, K. Cicak, J. Aumentado, S. A. Diddams, and J. D. Teufel, "Control and Readout of a Superconducting Qubit Using a Photonic Link," *Nature* 591 (2021): 575–579, https://doi.org/10.1038/s41586-021-03268-x.

4. G. Arnold, T. Werner, R. Sahu, L. N. Kapoor, L. Qiu, and J. M. Fink, "All-optical Superconducting Qubit Readout," *Nature Physics* 21 (2025): 393–400, https://doi.org/10.1038/s41567-024-02741-4.

5. H. K. Warner, J. Holzgrafe, B. Yankelevich, et al., "Coherent Control of a Superconducting Qubit Using Light," *Nature Physics* 21 (2025): 831–838.

6. C. Wang, I. Gonin, A. Grassellino, et al., "High-Efficiency Microwave-Optical Quantum Transduction Based on a Cavity Electro-Optic Superconducting System With Long Coherence Time," *npj Quantum Inf* 8 (2022): 149.

7. PsiQuantum team, "A manufacturable platform for photonic quantum computing," *Nature* 641 (2025): 876883, https://doi.org/10.1038/s41586-025-08820-7.

8. A. R. Johnston and J. M. Weingart, "Determination of the Low-Frequency Linear Electro-Optic Effect in Tetragonal $BaTiO_3$†," *Journal of the Optical Society of America* 55 (1965): 828, https://doi.org/10.1364/JOSA.55.000828.

9. S. Abel, F. Eltes, J. E. Ortmann, et al., "Large Pockels Effect in Micro- and Nanostructured Barium Titanate Integrated on Silicon," *Nature Materials* 18 (2019): 42–47, https://doi.org/10.1038/s41563-018-0208-0.

10. A. R. Johnston, "Dispersion of Electro-Optic Effect in BaTiO3," *Journal of Applied Physics* 42 (1971): 3501–3507, https://doi.org/10.1063/1.1660761.

11. A. Ross, M. S. M. M. Ali, A. Saha, et al., "Thermodynamic Theory of Linear Optical and Electro-optical Properties of Ferroelectrics," *Physical Review B* 111 (2025): 085109, https://doi.org/10.1103/PhysRevB.111.085109.

12. I. Kim, T. Paoletta, and A. A. Demkov, "Nature of Electro-optic Response in Tetragonal BaTiO3," *Physical Review B* 108 (2023): 115201, https://doi.org/10.1103/PhysRevB.108.115201.

13. F. Eltes, G. E. Villarreal-Garcia, D. Caimi, et al., "An Integrated Optical Modulator Operating at Cryogenic Temperatures," *Nature Materials* 19 (2020): 1164–1168, https://doi.org/10.1038/s41563-020-0725-5.

14. E. K. H. Salje, B. Wruck, and H. Thomas, "Order-parameter Saturation and Low-temperature Extension of Landau Theory," *Zeitschrift fur Physik B Condensed Matter* 82 (1991): 399–404, https://doi.org/10.1007/BF01357186.

15. K. A. Müller and H. Burkard, "$SrTiO_3$: An Intrinsic Quantum Paraelectric below 4 K," *Physical Review B* 19 (1979): 3593–3602, https://doi.org/10.1103/PhysRevB.19.3593.

16. U. T. Höchli, H. E. Weibel, and L. A. Boatner, "Quantum Limit of Ferroelectric Phase Transitions in KTa1−xNbxO_3," *Physical Review Letters* 39 (1977): 1158–1161, https://doi.org/10.1103/PhysRevLett.39.1158.

17. T. Esswein and N. A. Spaldin, "Ferroelectric, Quantum Paraelectric, or Paraelectric? Calculating the Evolution from $BaTiO_3$ to $SrTiO_3$ to $KTaO_3$ Using a Single-particle Quantum Mechanical Description of the Ions," *Physical Review Research* 4 (2022): 033020, https://doi.org/10.1103/PhysRevResearch.4.033020.

18. S. A. Hayward and E. K. H. Salje, "The Pressure–Temperature Phase Diagram of $BaTiO_3$: A Macroscopic Description of the Low-Temperature Behaviour," *Journal of Physics-Condensed Matter* 14 (2002): L599.

19. A. Suceava, S. Hazra, A. Ross, et al., "Colossal Cryogenic Electro-Optic Response through Metastability in Strained $BaTiO_3$ Thin Films," *Advanced Materials* 38 (2026): 07564, https://doi.org/10.1002/adma.202507564.

20. J. W. Matthews and A. E. Blakeslee, "Defects in epitaxial multilayers: I. Misfit dislocations," *Journal of Crystal Growth* 27 (1974): 118.

21. R. People and J. C. Bean, "Calculation of Critical Layer Thickness Versus Lattice Mismatch for Ge X Si1− X/Si Strained-Layer Heterostructures," *Applied Physics Letters* 47 (1985): 322–324, https://doi.org/10.1063/1.96206.

22. J.-M. Liu, *Photonic Devices* (Cambridge University Press).

23. J. H. Barrett, "Dielectric Constant in Perovskite Type Crystals," *Physical Review* 86 (1952): 118–120, https://doi.org/10.1103/PhysRev.86.118.

24. C. P. Anderson, G. Scuri, A. Chan, et al., "Quantum Critical Electro-Optic and Piezo-Electric Nonlinearities," *Science* 390 (2025): 394–399, https://doi.org/10.1126/science.adx8657.

25. Y. L. Li, L. E. Cross, and L. Q. Chen, "A Phenomenological Thermodynamic Potential for BaTiO3 Single Crystals," *Journal of Applied Physics* 98 (2005): 064101, https://doi.org/10.1063/1.2042528.

26. H. Fu and R. E. Cohen, "Polarization Rotation Mechanism for Ultrahigh Electromechanical Response in Single-Crystal Piezoelectrics," *Nature* 403 (2000): 281–283, https://doi.org/10.1038/35002022.

27. B. Noheda, J. A. Gonzalo, L. E. Cross, et al., "Tetragonal-to-monoclinic Phase Transition in a Ferroelectric Perovskite: The Structure of PbZr0.52Ti0.48O3," *Physical Review B* 61 (2000): 8687–8695, https://doi.org/10.1103/PhysRevB.61.8687.

28. H. Cao, C. P. Devreugd, W. Ge, et al., "Monoclinic MC Phase in (001) Field Cooled $BaTiO_3$ Single Crystals," *Applied Physics Letters* 94 (2009): 032901, https://doi.org/10.1063/1.3073716.

29. T. T. A. Lummen, Y. Gu, J. Wang, et al., "Thermotropic Phase Boundaries in Classic Ferroelectrics," *Nature Communications* 5 (2014): 3172, https://doi.org/10.1038/ncomms4172.

30. C. Eisenschmidt, H. T. Langhammer, R. Steinhausen, and G. Schmidt, "Tetragonal-Orthorhombic Phase Transition in Barium Titanate via Monoclinic M C Type Symmetry," *Ferroelectrics* 432 (2012): 103–116, https://doi.org/10.1080/00150193.2012.707894.

31. M. DiDomenico and S. H. Wemple, "Oxygen-Octahedra Ferroelectrics. I. Theory of Electro-optical and Nonlinear Optical Effects," *Journal of Applied Physics* 40 (1969): 720–734, https://doi.org/10.1063/1.1657458.

32. J. Dec and W. Kleemann, "From barrett to Generalized Quantum Curie–Weiss Law," *Solid State Communications* 106 (1998): 695–699, https://doi.org/10.1016/S0038-1098(98)00072-6.

33. D. Fu, M. Itoh, S. Koshihara, T. Kosugi, and S. Tsuneyuki, "Anomalous Phase Diagram of Ferroelectric (Ba,Ca)TiO_3 Single Crystals With Giant Electromechanical Response," *Physical Review Letters* 100 (2008): 227601, https://doi.org/10.1103/PhysRevLett.100.227601.

34. M. Iwata, Z. Kutnjak, Y. Ishibashi, and R. Blinc, "Consideration on the Phase Diagrams of Ferroelectric (Ba,Ca)TiO_3," *Journal of the Physical Society of Japan* 78 (2009): 054706, https://doi.org/10.1143/JPSJ.78.054706.

35. R. C. DeVries and R. Roy, "Phase Equilibria in the System $BaTiO_3$—$CaTiO_3$," *Journal of the American Ceramic Society* 38 (1955): 142–146, https://doi.org/10.1111/j.1151-2916.1955.tb14918.x.

36. C. Kuper, R. Pankrath, and H. Hesse, "Growth and Dielectric Properties of Congruently Melting Ba 1-x Ca X TiO_3 Crystals," *Applied Physics A: Materials Science & Processing* 65 (1997): 301–305, https://doi.org/10.1007/s003390050583.

37. L. B. Barbosa, D. R. Ardila, and J. P. Andreeta, "Crystal Growth of Congruent Barium Calcium Titanate by LHPG," *Journal of Crystal Growth* 231 (2001): 488–492, https://doi.org/10.1016/S0022-0248(01)01455-5.

38. D. Fu, M. Itoh, and S. Koshihara, "Crystal Growth and Piezoelectricity of $BaTiO_3$–$CaTiO_3$ Solid Solution," *Applied Physics Letters* 93 (2008): 012904, https://doi.org/10.1063/1.2956400.

39. A. C. Victor, "Heat Capacity of Diamond at High Temperatures," *Journal of Chemical Physics* 36 (1962): 1903.

40. J. M. Pérez-Mato and E. K. H. Salje, "Order-parameter Saturation at Low Temperatures: Displacive Phase Transitions with Coupled Einstein Oscillators," *Philosophical Magazine Letters* 81 (2001): 885–891, https://doi.org/10.1080/09500830110089961.

15214095, 0, Downloaded from https://advanced.onlinelibrary.wiley.com/doi/10.1002/adma.75543, Wiley Online Library on [16/11/2026]. See the Terms and Conditions (https://onlinelibrary.wiley.com/terms-and-conditions) on Wiley Online Library for rules of use; OA articles are governed by the applicable Creative Commons License

41. Y. L. Li, S. Y. Hu, Z. K. Liu, and L. Q. Chen, "Effect of Substrate Constraint on the Stability and Evolution of Ferroelectric Domain Structures in Thin Films," *Acta Materialia* 50 (2002): 395–411, https://doi.org/10.1016/S1359-6454(01)00360-3.

42. R. Uecker, B. Velickov, D. Klimm, et al., "Properties of Rare-earth Scandate Single Crystals (Re = Nd−Dy)," *Journal of Crystal Growth* 310 (2008): 2649–2658, https://doi.org/10.1016/j.jcrysgro.2008.01.019.

43. X. Cheng, "MUPRO," can be found under https://mupro.co/, **n.d**.

44. T. Shimizu, D. Fu, H. Taniguchi, T. Taniyama, and M. Itoh, "Origin of the Dielectric Response in $Ba0.767Ca0.233TiO_3$," *Applied Physics Letters* 100 (2012): 102908, https://doi.org/10.1063/1.3693524.

45. M. E. Savinov, V. A. Trepakov, S. Kamba, et al., "Dielectric and Infrared Response of $Ba0.77Ca0.23TiO_3$," *Ferroelectrics* 295 (2003): 31.

Supporting Information

Additional supporting information can be found online in the Supporting Information section.

Supporting File: adma75543-sup-0001-SuppMat.docx.

15214095, 0, Downloaded from https://advanced.onlinelibrary.wiley.com/doi/10.1002/adma.75543, Wiley Online Library on [16/11/2026]. See the Terms and Conditions (https://onlinelibrary.wiley.com/terms-and-conditions) on Wiley Online Library for rules of use; OA articles are governed by the applicable Creative Commons License

Supporting Information

Quantum Saturation of the Electro-Optic Effect

Aiden Ross, Sankalpa Hazra, Albert Suceava, Dylan Sotir, Ian Reed Philippi, Darrell G. Schlom, Venkatraman Gopalan, and Long-Qing Chen**

Supplemental Note 1: Parameters in the thermodynamic free-energy function for $BaTiO_3$

For $BaTiO_3$, we use the cubic phase ($m\bar{3}m$) as our high symmetry reference state and employ an 8th-order landau expansion to describe the relative stability of the lattice polarization compared to the cubic reference state. The coefficients used for this paper are adjusted from Li *et al.*[1] and Ross *et al.*[2] to include the effect of quantum fluctuations and are given in Table S1.

Table S1. Coefficients in the thermodynamic free energy function and equation of motion for $BaTiO_3$

g_{1111}^{LL}	$18.5 \times 10^{-2}(\mathrm{m^4/C^2})$	p_{1111}	0.5328 (Unitless)
g_{1122}^{LL}	$2.5 \times 10^{-2}(\mathrm{m^4/C^2})$	p_{1122}	0.1584 (Unitless)
g_{1212}^{LL}	$12.85 \times 10^{-2}(\mathrm{m^4/C^2})$	p_{1212}	-0.432 (Unitless)
μ_e	$35.5 \times 10^{-23}\left(\frac{\mathrm{Kg}}{\mathrm{m}}\frac{\mathrm{m^4}}{\mathrm{C^2}}\right)$	γ_e	$3 \times 10^{-9}\left(\frac{\mathrm{Kg}}{\mathrm{ms}}\frac{\mathrm{m^4}}{\mathrm{C^2}}\right)$
a_{11}	$a_0\, T_s\left(\coth\left(\frac{T_s}{T}\right) - \coth(\frac{T_s}{T_c})\right)$	$B_{ij}^{e,ref}(T_0)$	0.2356 (Unitless)
T_c	388 K	T_0	398 K
T_s	54 K	a_0	$4.124 \times 10^5\left(\frac{\mathrm{J}}{\mathrm{m^3}}\ \frac{\mathrm{m^4}}{\mathrm{K\,C^2}}\right)$
a_{1111}	$-2.097 \times 10^8\left(\frac{\mathrm{J}}{\mathrm{m^3}}\ \frac{\mathrm{m^8}}{\mathrm{C^4}}\right)$	α_{11}	$2.657 \times 10^{-5}\left(\frac{1}{\mathrm{K}}\right)$
a_{1122}	$7.974 \times 10^8\left(\frac{\mathrm{J}}{\mathrm{m^3}}\ \frac{\mathrm{m^8}}{\mathrm{C^4}}\right)$	$a_{11111111}$	$3.863 \times 10^{10}\left(\frac{\mathrm{J}}{\mathrm{m^3}}\ \frac{\mathrm{m^{16}}}{\mathrm{C^8}}\right)$
a_{111111}	$1.294 \times 10^9\left(\frac{\mathrm{J}}{\mathrm{m^3}}\ \frac{\mathrm{m^{12}}}{\mathrm{C^6}}\right)$	$a_{11111122}$	$2.529 \times 10^{10}\left(\frac{\mathrm{J}}{\mathrm{m^3}}\ \frac{\mathrm{m^{16}}}{\mathrm{C^8}}\right)$
a_{111122}	$-1.95 \times 10^9\left(\frac{\mathrm{J}}{\mathrm{m^3}}\ \frac{\mathrm{m^{12}}}{\mathrm{C^6}}\right)$	$a_{11112222}$	$1.637 \times 10^{10}\left(\frac{\mathrm{J}}{\mathrm{m^3}}\ \frac{\mathrm{m^{16}}}{\mathrm{C^8}}\right)$
a_{112233}	$-2.509 \times 10^9\left(\frac{\mathrm{J}}{\mathrm{m^3}}\ \frac{\mathrm{m^{12}}}{\mathrm{C^6}}\right)$	$a_{11112233}$	$1.367 \times 10^{10}\left(\frac{J}{m^3}\ \frac{m^{16}}{C^8}\right)$
C_{11}	1.78×10^{11} Pa	C_{44}	1.22×10^{11} Pa
C_{12}	0.964×10^{11} Pa	Q_{11}	$0.11\ (\mathrm{m^4/C^2})$
Q_{12}	$-0.045\ (\mathrm{m^4/C^2})$	Q_{44}	$0.029\ (\mathrm{m^4/C^2})$

Supplemental Note 2: Parameters in the thermodynamic free-energy function for $Ba_{1-x}Ca_xTiO_3$

For $Ba_{1-x}Ca_xTiO_3$, we use the cubic phase ($m\bar{3}m$) as our high symmetry reference state and employ an 8th-order landau expansion to describe the relative stability of the lattice polarization compared to the cubic reference state. The thermodynamic coefficients for $Ba_{1-x}Ca_xTiO_3$ are given in table S2 and were fit to experimental measurements of the spontaneous polarization, phase transition temperatures and dielectric constants.[3–6] For simplicity, we ignore the composition dependence of the quadratic polar-optic tensor, and reference electronic dielectric stiffness and use the values obtained for $BaTiO_3$. The coefficients used for $Ba_{1-x}Ca_xTiO_3$ are given in Table S2.

Table S2. Coefficients in the thermodynamic free energy function and equation of motion for $Ba_{1-x}Ca_xTiO_3$

g_{1111}^{LL}	$18.5 \times 10^{-2}(\mathrm{m}^4/\mathrm{C}^2)$	p_{1111}	0.5328 (Unitless)
g_{1122}^{LL}	$2.5 \times 10^{-2}(\mathrm{m}^4/\mathrm{C}^2)$	p_{1122}	0.1584 (Unitless)
g_{1212}^{LL}	$12.85 \times 10^{-2}(\mathrm{m}^4/\mathrm{C}^2)$	p_{1212}	-0.432 (Unitless)
μ_e	$35.5 \times 10^{-23}\left(\frac{\mathrm{Kg}}{\mathrm{m}}\frac{\mathrm{m}^4}{\mathrm{C}^2}\right)$	γ_e	$3 \times 10^{-9}\left(\frac{\mathrm{Kg}}{\mathrm{ms}}\frac{\mathrm{m}^4}{\mathrm{C}^2}\right)$
a_{11}	$a_0\, T_s\left(\coth\left(\frac{T_s}{T}\right) - \coth(\frac{T_s}{T_c})\right)$	$B_{ij}^{e,ref}(T_0)$	0.2356 (Unitless)
T_c	$390(1-x) + 340x$ K	T_0	398 K
T_s	140 K	a_0	$4.124 \times 10^5\left(\frac{\mathrm{J}}{\mathrm{m}^3}\ \frac{\mathrm{m}^4}{\mathrm{K\,C}^2}\right)$
a_{1111}	$-2.097 \times 10^8(1-6.0x)\left(\frac{\mathrm{J}}{\mathrm{m}^3}\ \frac{\mathrm{m}^8}{\mathrm{C}^4}\right)$	α_{11}	$2.657 \times 10^{-5}\left(\frac{1}{\mathrm{K}}\right)$
a_{1122}	$7.974 \times 10^8(1 + 3.6x + 7.0x^2)\left(\frac{\mathrm{J}}{\mathrm{m}^3}\ \frac{\mathrm{m}^8}{\mathrm{C}^4}\right)$	$a_{11111111}$	$3.863 \times 10^{10}\left(\frac{\mathrm{J}}{\mathrm{m}^3}\ \frac{\mathrm{m}^{16}}{\mathrm{C}^8}\right)$
a_{111111}	$1.294 \times 10^9\left(\frac{\mathrm{J}}{\mathrm{m}^3}\ \frac{\mathrm{m}^{12}}{\mathrm{C}^6}\right)$	$a_{11111122}$	$2.529 \times 10^{10}\left(\frac{\mathrm{J}}{\mathrm{m}^3}\ \frac{\mathrm{m}^{16}}{\mathrm{C}^8}\right)$
a_{111122}	$-1.75 \times 10^9(1+5.0x)\left(\frac{\mathrm{J}}{\mathrm{m}^3}\ \frac{\mathrm{m}^{12}}{\mathrm{C}^6}\right)$	$a_{11112222}$	$1.637 \times 10^{10}\left(\frac{\mathrm{J}}{\mathrm{m}^3}\ \frac{\mathrm{m}^{16}}{\mathrm{C}^8}\right)$
a_{112233}	$-2.509 \times 10^9(1+32x)\left(\frac{\mathrm{J}}{\mathrm{m}^3}\ \frac{\mathrm{m}^{12}}{\mathrm{C}^6}\right)$	$a_{11112233}$	$1.367 \times 10^{10}\left(\frac{\mathrm{J}}{\mathrm{m}^3}\ \frac{\mathrm{m}^{16}}{\mathrm{C}^8}\right)$

Supplemental Note 3: Quantifying Strain in $BaTiO_3$ grown on $GdScO_3$

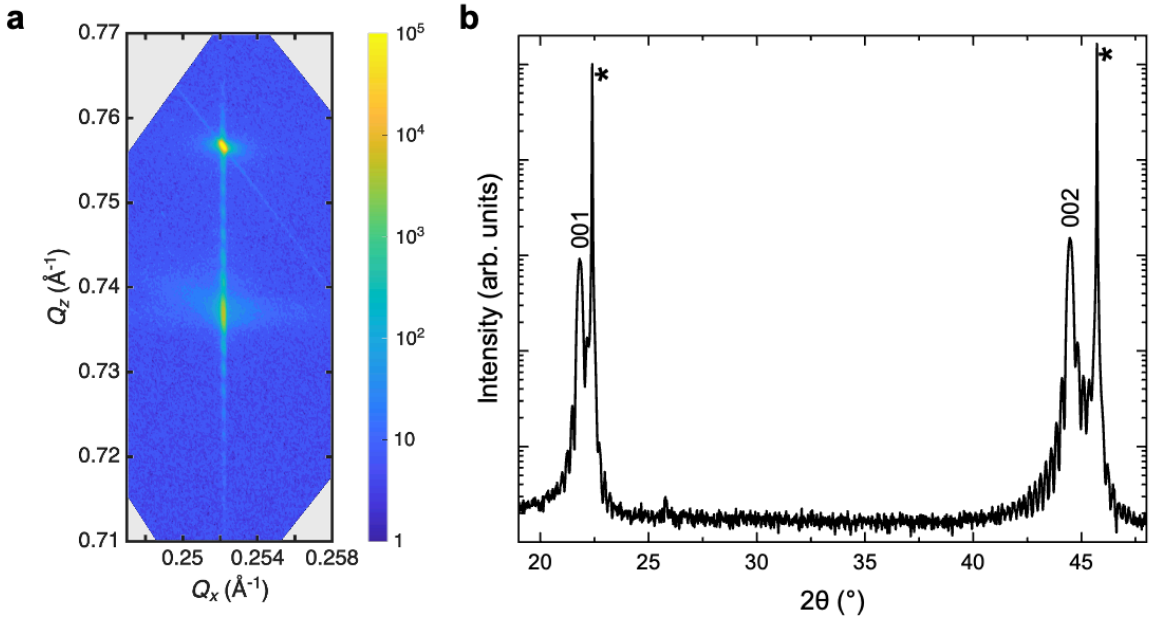


Figure S1. a) Asymmetric reciprocal space map scan taken at the $GdScO_3$ 332 peak, demonstrating epitaxial growth. b) θ-2θ x-ray diffraction scan showing an approximately 37 nm thick film of $BaTiO_3$ grown on $GdScO_3$ $(110)_o$ at T_{sub} = 1160 °C at a background pressure of 10% ozone of 1×10^{-6} Torr.

Given the strong strain dependence of the electro-optic coefficient, it is important to properly quantify and calibrate the value of strain on both the simulated and experimental film. If the film is commensurately strained to the substrate, then the in-plane strain can be directly determined using the equivalent cubic lattice parameters for $BaTiO_3$ and the pseudocubic lattice parameters for $GdScO_3$

$$\varepsilon_{11} = \frac{a^{GSO_{1\bar{1}0}} - a^{eq}}{a^{eq}}, \varepsilon_{22} = \frac{a^{GSO_{001}} - a^{eq}}{a^{eq}} \quad \text{(S1)}$$

Where a^{eq} is the equivalent cubic lattice parameter of a stress-free, polarization-free, cubic $BaTiO_3$, and $a^{GSO_{1\bar{1}0}}$ and $a^{GSO_{001}}$ are the pseudocubic lattice parameters of the $GdScO_3$ substrate. The reciprocal space map indicates that the film is commensurately strained to the substrate.

We can further validate the imposed strain by calculating the theoretically predicted lattice parameters from thermodynamic analysis and comparing them against the experimentally measured lattice parameters extracted from a reciprocal space map. The theoretically predicted the *c*-axis lattice parameter for $BaTiO_3$ commensurately strained to $GdScO_3$ is 4.073 Å at 293 K, which closely matches the *c*-axis lattice parameter, measured from the reciprocal space mapping, 4.073 ± 0.003 Å, where $\varepsilon_{11} = -0.94\%, \varepsilon_{22} = -1.04\%$ at 293 K (see **Supplementary Note 4** for the full derivation).

Supplemental Note 4: Prediction of Lattice Parameters from Thermodynamic Analysis

Based on the Landau-Ginzburg-Devonshire Theory of Ferroelectrics, the Gibbs free energy density of $BaTiO_3$ can be written as a power series of the polarization. For simplicity, we will only consider the normal components of stress and strain

$$\begin{aligned} g(T,P,\sigma) = {} & a_1(T)(P_1^2+P_2^2+P_3^2) + a_{11}(P_1^4+P_2^4+P_3^4) \\ & + a_{12}(P_2^2P_3^2+P_1^2P_3^2+P_1^2P_2^2) + a_{111}(P_1^6+P_2^6+P_3^6) \\ & + a_{112}\big(P_1^4(P_2^2+P_3^2)+P_2^4(P_1^2+P_3^2)+P_3^4(P_1^2+P_2^2)\big) + a_{123}P_1^2P_2^2P_3^2 \\ & + a_{1111}(P_1^8+P_2^8+P_3^8) \\ & + a_{1112}\big(P_1^6(P_2^2+P_3^2)+P_2^6(P_1^2+P_3^2)+P_3^6(P_1^2+P_2^2)\big) \\ & + a_{1122}(P_1^4P_2^4+P_2^4P_3^4+P_3^4P_1^4) + a_{1123}(P_1^4P_2^2P_3^2+P_1^2P_2^4P_3^2 \\ & + P_1^2P_2^2P_3^4) \\ & -\tfrac{1}{2}S_{11}(\sigma_1^2+\sigma_2^2+\sigma_3^2) - S_{12}(\sigma_2\sigma_3+\sigma_1\sigma_3+\sigma_1\sigma_2) \\ & -Q_{11}(\sigma_1P_1^2+\sigma_2P_2^2+\sigma_3P_3^2) - Q_{12}((\sigma_2+\sigma_3)P_1^2+(\sigma_1+\sigma_3)P_2^2+(\sigma_1+\sigma_2)P_3^2), \end{aligned} \tag{S2}$$

where T is temperature, P_i is polarization, σ_i is stress in Voigt notation, a_1, a_{11}, a_{12} ... are the dielectric stiffness coefficients measured under constant stress, S_{ij} is the elastic compliance tensor of the paraelectric phase under a constant dielectric displacement in Voigt notation, and Q_{ij} is the electrostrictive tensor in condensed 2-index matrix form.

For a ferroelectric thin film epitaxially grown on a substrate, we may assume that the in-plane strains are fixed by the lattice parameter of the substrate and the out-of-plane components of stress are free to relax. Therefore, the in-plane components of strain $(\varepsilon_1, \varepsilon_2)$ and the out-of-plane components of stress (σ_3) will be independent variables, leaving the in-plane components of stress (σ_1, σ_2) and the out-of-plane components of strain (ε_3) as dependent variables. While equation S2 describes the thermodynamic behavior using stress as the independent variable and strain as the dependent variable, we can transform this equation to be more suitable for ferroelectric thin films, where the in-plane strain and out-of-plane stress are independent variables.

$$f(T,P_i,\varepsilon_1,\varepsilon_2,\sigma_3) = u - Ts - \sigma_3\varepsilon_3 = g + \sigma_1\varepsilon_1 + \sigma_2\varepsilon_2 \tag{S3}$$

To perform the Legendre transform, we must find $\sigma_1(T,P_i,\varepsilon_1,\varepsilon_2,\sigma_3)$ and $\sigma_2(T,P_i,\varepsilon_1,\varepsilon_2,\sigma_3)$. For simplicity we shall only consider the impact of normal strains. To do this we shall first calculate

$$\varepsilon_1(T,P_i,\sigma_1,\sigma_2,\sigma_3) = -\left(\frac{\partial g}{\partial \sigma_1}\right)_{T,P} = Q_{11}P_1^2 + Q_{12}(P_2^2+P_3^2) + S_{11}\sigma_1 + S_{12}(\sigma_2+\sigma_3) \tag{S4}$$

$$\varepsilon_2(T,P_i,\sigma_1,\sigma_2,\sigma_3) = -\left(\frac{\partial g}{\partial \sigma_2}\right)_{T,P} = Q_{11}P_2^2 + Q_{12}(P_1^2+P_3^2) + S_{11}\sigma_2 + S_{12}(\sigma_1+\sigma_3) \tag{S5}$$

Then algebraically solve for $\sigma_1(T,P_i,\varepsilon_1,\varepsilon_2,\sigma_3)$ and $\sigma_2(T,P_i,\varepsilon_1,\varepsilon_2,\sigma_3)$,

$$\begin{aligned} & \sigma_1(T,P_i,\varepsilon_1,\varepsilon_2,\sigma_3) \\ & = \frac{\varepsilon_1 - \left(Q_{11}P_1^2 + Q_{12}(P_2^2+P_3^2)\right) - \left(S_{12} - \frac{S_{12}^2}{S_{11}}\right)\sigma_3 + \frac{S_{12}}{S_{11}}(Q_{11}P_2^2 + Q_{12}(P_1^2+P_3^2) - \varepsilon_2)}{S_{11} - \frac{S_{12}^2}{S_{11}}} \end{aligned} \tag{S6}$$

$$\sigma_2(T, P_i, \varepsilon_1, \varepsilon_2, \sigma_3) = \frac{\varepsilon_2 - \left(Q_{11}P_2^2 + Q_{12}(P_1^2 + P_3^2)\right) - \left(S_{12} - \frac{S_{12}^2}{S_{11}}\right)\sigma_3 + \frac{S_{12}}{S_{11}}(Q_{11}P_1^2 + Q_{12}(P_2^2 + P_3^2) - \varepsilon_1)}{S_{11} - \frac{S_{12}^2}{S_{11}}} \quad \text{(S7)}$$

Substituting in these expressions for σ_1 and σ_2 in equation S10 we obtain an expression that uses the in-plane strain and the out-of-plane stress as the independent variables.

$$\tilde{f}(T, P_i, \varepsilon_1, \varepsilon_2, \sigma_3) = g(T, P_i,\ \sigma_1(T, P_i, \varepsilon_1, \varepsilon_2, \sigma_3),\ \sigma_2(T, P_i, \varepsilon_1, \varepsilon_2, \sigma_3),\ \sigma_3) + \sigma_1(T, P_i, \varepsilon_1, \varepsilon_2, \sigma_3)\varepsilon_1 + \sigma_2(T, P_i, \varepsilon_1, \varepsilon_2, \sigma_3)\varepsilon_2 \quad \text{(S8)}$$

Where the out-of-plane strain is

$$\varepsilon_3 = -\left(\frac{\partial \tilde{f}}{\partial \sigma_3}\right)_{T, P_i, \varepsilon_1, \varepsilon_2}. \quad \text{(S9)}$$

If we assume that we have a tetragonal C domain ($P_i = (0, 0, P_3)$ the out-of-plane strain is

$$\varepsilon_3 = \frac{(\varepsilon_1 + \varepsilon_2)S_{12}}{S_{11} + S_{12}} + \left(Q_{11} - \frac{2Q_{12}S_{12}}{S_{11} + S_{12}}\right)P_3^2 \quad \text{(S10)}$$

Then to get the lattice parameter one can use the relation

$$\varepsilon_3 = \frac{c - a^{eq}}{a^{eq}} \quad \text{(S11)}$$

Where a^{eq} is the equivalent cubic lattice parameter of a stress-free, polarization-free, cubic $BaTiO_3$. Using this we find

$$c = a^{eq}\left[1 + \frac{(\varepsilon_1 + \varepsilon_2)S_{12}}{S_{11} + S_{12}} + \left(Q_{11} - \frac{2Q_{12}S_{12}}{S_{11} + S_{12}}\right)P_3^2\right], \quad \text{(S12)}$$

Where the misfit strain is calculated using the equivalent cubic lattice parameters for $BaTiO_3$ and the pseudocubic lattice parameters for $GdScO_3$

$$\varepsilon_1 = \frac{a^{GSO_{1\bar{1}0}} - a^{eq}}{a^{eq}}, \varepsilon_2 = \frac{a^{GSO_{001}} - a^{eq}}{a^{eq}} \quad \text{(S13)}$$

and the polarization is found by solving

$$\left(\frac{\partial \tilde{f}}{\partial P_3}\right)_{T, \varepsilon_1, \varepsilon_2, \sigma_3} = 0. \quad \text{(S14)}$$

Supplemental Note 5: Critical Thickness of Strained $BaTiO_3$

For a strained thin film, beyond a certain thickness it becomes more energetically favorable to introduce a dislocation to relieve the strain on the system. $BaTiO_3$ has been demonstrated to slip on both the {110}<1$\bar{1}$0> and the {100}<001> systems, but the {100}<001> system is dominant at high temperatures, so it is the more relevant system under these conditions[7]. Using the Matthews-Blakeslee criterion[8] from the derivation in[9]:

$$h_{cr} = \frac{1}{|\epsilon_m|(1+\nu)} \frac{b}{8\pi \cos(\lambda)} (1 - \nu cos^2(\beta)) ln \frac{\alpha h_{cr}}{b} \quad \text{(S15)}$$

Where h_{cr} is the theoretical critical thickness of dislocation formation, ϵ_m is the misfit strain, b is the magnitude of the Burgers vector, ν is Poisson's ratio, β is the angle between the line of the dislocation and the Burgers vector, λ is the angle between the Burgers vector and the interface, and α is the cutoff parameter. Assuming the {100}<001> slip system is dominant: ν is 0.23[10], β is 90°, λ is 0°, and α is 4[9]. We can therefore calculate the critical thickness for the range of misfit strains 0.8-0.9% to be approximately 5.9-6.8 nm.

While this limits the thickness of any potential strained material, this criterion does not consider several factors. First, this criterion estimates the thickness at which the formation of a single threading dislocation is energetically favorable, but to fully relax the film, several dislocations must form to fully compensate the misfit strain, therefore, full relaxation may occur in films with a far greater film thickness, and further study may be needed to understand the relationship between film thickness, dislocation density, and electro-optic coefficient. Second, the kinetics of dislocation formation are not considered, which serves as an additional barrier for strain relaxation. While prior researchers have observed much greater critical thicknesses than predicted due to kinetic barriers[11], the high homologous temperature of the film growth featured here may overcome those barriers. This would lower the critical thickness to more closely align with theory. Finally, the formation of ferroelectric domains in oxide thin films, and specifically $BaTiO_3$, has been shown to increase the critical thickness[12,13]. Due to these factors, we interpret the predicted critical thickness as a lower bound, and any future work on realizing devices with the exceptional properties predicted here could benefit from a study of the film relaxation.

Supplemental Note 6: Electro-optic Measurements

The $BaTiO_3$ on $GdScO_3$ sample used in this study constitutes a 37 nm thick $BaTiO_3$ film commensurately strained on a $GdScO_3$ single crystal substrate. At room temperature, this imparts a biaxial compressive strain, $\epsilon \sim -1.01$ % on the $BaTiO_3$ film resulting in a tetragonal phase (space group P4*mm*) with out-of-plane polarization. This transitions into a monoclinic phase (P*m*) at low temperature (< 50 K). The thin-film growth, structural characterization and phase transitions are further elaborated elsewhere[14]. The $BaTiO_3$ sample was not electrically poled prior to the measurements. The electro-optic response was measured in the as grown state. Although the samples were not poled, we suspect a net out of plane polarization is caused by an asymmetry of the interfaces on the top and bottom surfaces of $BaTiO_3$.

Electro-optic measurements were performed using a polarizer-sample-compensator-analyzer (PSCA) setup[14–16]. In this method the change in transmission of light through a pair of crossed polarizers is measured as a function of an applied AC electric field (E_{AC}) to the sample to quantify the field induced changed in refractive index. A schematic of the setup used for measurements is shown in **Figure S2**.

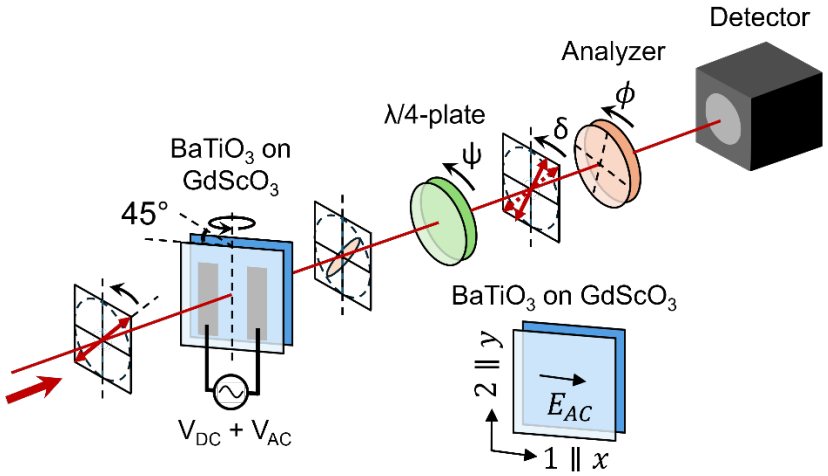


Figure S2: Schematic of the polarizer-sample-compensator-analyzer setup used for the electro-optic measurements. Inset shows the relationship between the crystal physics axes (1,2,3) of $BaTiO_3$ and the laboratory axes (x, y, z).

For the tetragonal phase of compressively strained $BaTiO_3$ films the [001] crystallographic direction lies out-of-plane. The crystal physics 1, 2, and 3 directions are conveniently aligned with the crystallographic [100], [010], and [001] directions and are aligned with the laboratory axes (x, y, z). 500 μm square electrodes comprising of 150 nm Pt with a 5 nm Ti adhesion layer were deposited with 200 μm spacing to apply electric field along the [100] direction (**Figure S3**).

The incident polarization is set to lie between two principal optic axes of the sample, which in this study are the [100] and [010] in-plane crystallographic axes of the $BaTiO_3$ film. With an in-plane electric field $E_1 (= E_{AC})$ along the [100] crystallographic direction of $BaTiO_3$ the index ellipsoid of the tetragonal phase distorts taking the original 1, 2, and 3 principal axes to a new set of axes: 1′, 2′ = 2, 3′:

$$\frac{x^2}{n_1^2}+\frac{y^2}{n_2^2}+\frac{z^2}{n_3^2}+2xzr_{51}E_1=1 \quad \text{(S16)}$$

In the absence of an external electric field, $x \equiv 1, y \equiv 2, z \equiv 3$ are the principal crystal physics axes, and with $n_1 = n_2 = n_o$ and $n_3 = n_e$ are the principal refractive indices. The action of r_{51} would lead to new principal crystal coordinates in the $x-z$ plane, leading to $x' \equiv 1'$ and $z' \equiv 3'$ axes. The $y' \equiv 2' = y \equiv 2$ would remain unchanged under this field. The principal crystal coordinates and the refractive indices do not change in the $x-y$ plane as seen from equation 1. Hence, a normal incident probe would not sample any field induced change in refractive indices.

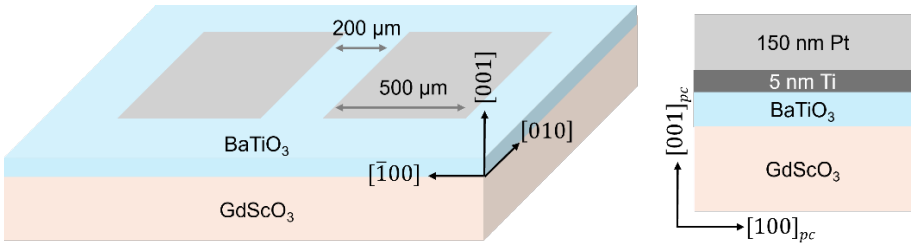


Figure S3: $500 \times 500\ \mu m^2$ electrodes with $200\ \mu m$ spacings are used for measurements. The electrodes constitute a 5 nm Ti adhesion layer and a 150 nm thick Pt layer. Measurements are made with a beam size of 40 µm.

The sample is tilted 45° away from the incident probe direction as shown in **Figure S2**. The 1550 nm probe beam experiences two orthogonal refractive indices n_o and $n_e(\theta_{film})$ without any voltage applied to the sample, and $n_o{}' = n_o$ and $n_e'(\theta_{film})$ when external voltage is applied to the sample, where θ_{film} is the refracted angle of the probe beam inside the film. Even without an external electric field, the native birefringence induced by the sample changes the probe beam polarization from linear to an elliptical state. A quarter-wave plate after the sample cancels out this natural material birefringence, along with any birefringence induced by the different optical elements used in the setup. The final linear polarized light is measured via an analyzer.

The unmodulated probe beam (without an external electric field applied to the sample) is described by;

$$I = I_0 \cos^2(\phi + \delta) \quad \text{(S17)}$$

where, ϕ represents the angle through which the analyzer is rotated and δ represents the overall phase accumulated by the probe beam transmission through the sample and other optical components as shown in **Figure S2** Under an applied electric field the modulated intensity, ΔI, can be expressed as;

$$\Delta I = I_0\, \Delta\delta\, \sin 2(\phi + \delta) \quad \text{(S18)}$$

where, $\Delta\delta$, represents the change in phase acquired by the probe beam due to electric field induced change in refractive index of the sample. Following **Equations S17** and **S18**, the change in phase, $\Delta\delta$, due to the change in refractive index of the film can be calculated as the ratio of amplitude of I and ΔI, $\Delta\delta = \Delta I/I$. Assuming a single pass through the film, the

measured $\Delta\delta$ can be related to the electric-field induced birefringence, $\Delta n = \frac{\Delta\delta\lambda}{2\pi L}$, where, $\lambda = 1550\ nm$ is the wavelength of the probe light used for measurements and $L = t/\cos(\theta_{film})$ is the path length of light travelled through the $BaTiO_3$ film. The film thickness, t, is determined to be 37 nm from spectroscopic ellipsometry and x-ray reflectivity measurements[14].

Figure S4 shows the Δn vs. E_{AC} curves measured at 6 K at 555 Hz, showing a nonlinear electro-optic response. The origin of such a response in the monoclinic phase of $BaTiO_3$ (below 50 K) is discussed further elsewhere[14]. By taking the maximum slope of the Δn vs. E_{AC} curve at the inflection point, the maximum achievable electro-optic response is calculated using, $r_{\text{eff}} = \frac{2\Delta n}{n_e(\theta_{film})^3 E_{AC}}$.

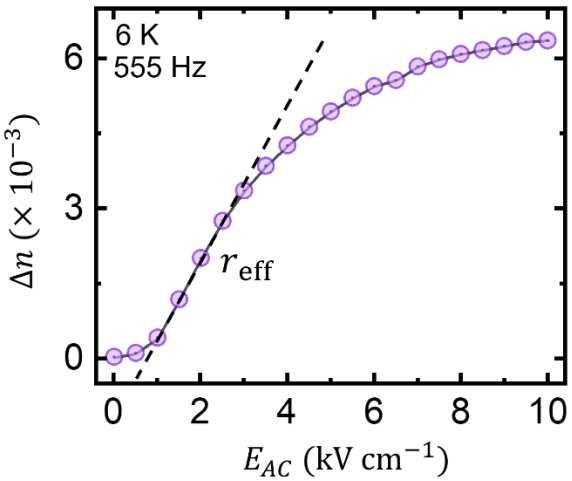


Figure S4: Δn vs. E_{AC} curves measured for $BaTiO_3$ on $GdScO_3$ at 6 K under a modulation frequency of 555 Hz. The slope at the inflection is represented by a dashed line.

Supplemental Note 7: Frequency Dependence of the Electro-Optic Response

To assess whether the measured electro-optic response is influenced by low-frequency effects additional measurements were performed over modulation frequencies ranging from 555 Hz to 100 kHz. As shown in **Figure S5a**, the measured electro-optic coefficient remains constant within ± 6% of the mean electro-optic coefficient within this frequency range. Furthermore, the measured change in the refractive index as a function of applied AC electric field exhibits nearly identical behavior at all measured frequencies (**Figure S5b**), indicating the underlying electro-optic response remains approximately frequency independent over this frequency range.

We note that the absolute electro-optic coefficient measured during this experimental run is lower than the peak value reported in the main text. Similar variability has been reported for this material system between different cooling runs. Despite this variation, the electro-optic coefficient remains near 1390 pm/V, well within the high electro-optic regime and therefore does not alter the conclusions regarding the frequency dependence of the electro-optic response.

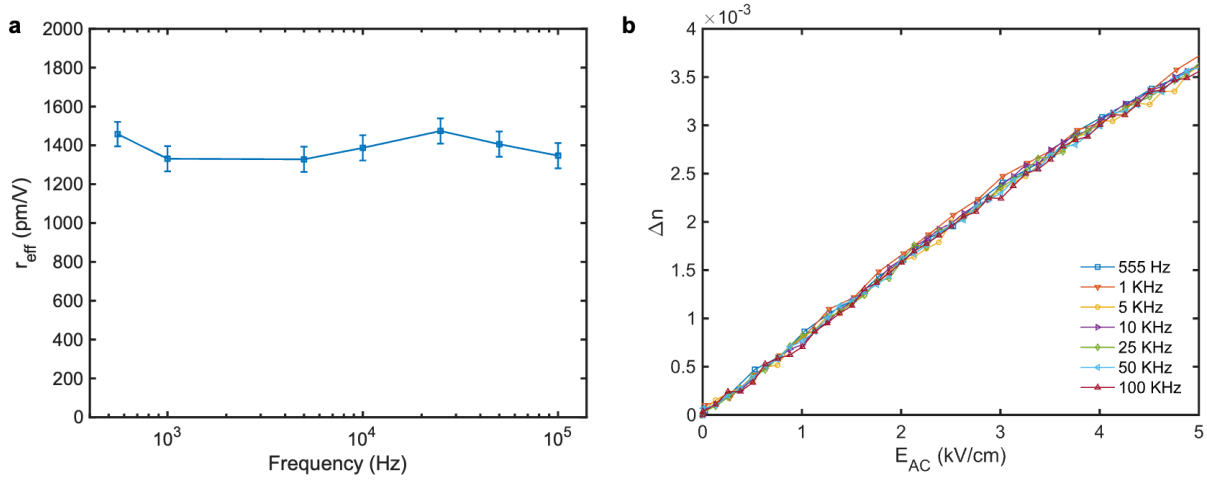


Figure S5. Frequency Dependent Electro-Optic Effect in $BaTiO_3$ on $GdScO_3$ a Effective electro-optic coefficient (r_{eff}) measured as a function of modulation frequency from 555 Hz to 100 KHz. **b,** Change in refractive index (Δn) as a function of the applied AC electric field amplitude measured at representative modulation frequencies.

References:

[1] Y. L. Li, L. E. Cross, L. Q. Chen, *Journal of Applied Physics* **2005**, *98*, 064101.
[2] A. Ross, M. S. M. M. Ali, A. Saha, R. Zu, V. Gopalan, I. Dabo, L.-Q. Chen, *Phys. Rev. B* **2025**, *111*, 085109.
[3] D. Fu, M. Itoh, S. Koshihara, T. Kosugi, S. Tsuneyuki, *Phys. Rev. Lett.* **2008**, *100*, 227601.
[4] M. Iwata, Z. Kutnjak, Y. Ishibashi, R. Blinc, *Journal of the Physical Society of Japan* **2009**, *78*, 054706.
[5] T. Shimizu, D. Fu, H. Taniguchi, T. Taniyama, M. Itoh, *Appl. Phys. Lett.* **2012**, *100*, 102908.
[6] M. E. Savinov, V. A. Trepakov, S. Kamba, S. E. Kapphan, J. Petzelt, R. Pankrath, I. L. Kislova, A. B. Kutsenko, L. Jastrabik, *Ferroelectrics* **2003**, *295*, 31.
[7] J.-P. Poirier, S. Beauchesne, F. Guyot, **n.d.**, DOI 10.1029/GM045p0119.
[8] J. W. Matthews, A. E. Blakeslee, *Journal of Crystal Growth* **1974**, *27*, 118.

[9] J. S. Speck, W. Pompe, *J. Appl. Phys.* **1994**, *76*, 466.
[10] M. de Jong, W. Chen, T. Angsten, A. Jain, R. Notestine, A. Gamst, M. Sluiter, C. Krishna Ande, S. van der Zwaag, J. J. Plata, C. Toher, S. Curtarolo, G. Ceder, K. A. Persson, M. Asta, *Sci Data* **2015**, *2*, 150009.
[11] B. W. Dodson, J. Y. Tsao, *Appl. Phys. Lett.* **1987**, *51*, 1325.
[12] Y. Zheng, B. Wang, C. H. Woo, *Appl. Phys. Lett.* **2006**, *89*, 083115.
[13] W. Pompe, X. Gong, Z. Suo, J. S. Speck, *J. Appl. Phys.* **1993**, *74*, 6012.
[14] A. Suceava, S. Hazra, A. Ross, I. R. Philippi, D. Sotir, B. Brower, L. Ding, Y. Zhu, Z. Zhang, H. Sarkar, S. Sarker, Y. Yang, S. Sarker, V. A. Stoica, D. G. Schlom, L.-Q. Chen, V. Gopalan, *Advanced Materials* **2026**, *38*, e07564.
[15] S. Abel, T. Stöferle, C. Marchiori, C. Rossel, M. D. Rossell, R. Erni, D. Caimi, M. Sousa, A. Chelnokov, B. J. Offrein, J. Fompeyrine, *Nat Commun* **2013**, *4*, 1671.
[16] M. Reynaud, M. Waqar, C. Du, A. B. Posadas, X. Pan, A. A. Demkov, *Commun Mater* **2025**, *6*, 176.